Modeling the vertical structure of the ice shelf-ocean boundary current under supercooled condition with suspended frazil ice processes: a case study underneath the Amery Ice Shelf, East Antarctica

Chen Cheng[*, a], Adrian Jenkins[b], Zhaomin Wang[c, a], Chengyan Liu[a, c]

[a]*Southern Marine Science and Engineering Guangdong Laboratory (Zhuhai), Zhuhai, 519000, China*

[b]*Department of Geography and Environmental Sciences, Northumbria University, Newcastle upon Tyne, NE1 8ST, UK*

[c]*College of Oceanography, Hohai University, Nanjing, 210098, China*

[*]Corresponding author.

E-mail address: icecheng1985@163.com (Chen Cheng).

Abstract: In contrast with the severe thinning of ice shelves along the coast of West Antarctica, large ice shelves (specifically, the Filchner-Ronne and Amery Ice Shelves) with deep grounding lines gained mass during the period 1994-2012. This positive mass budget is potentially associated with the marine ice production, which originates from the supercooled Ice Shelf Water plume carrying suspended frazil ice along the ice shelf base. In addition, the outflow of this supercooled plume from beneath the ice shelf arguably exerts a significant impact on the properties of Antarctic Bottom Water, as well as its production. However, knowledge of this buoyant and supercooled shear flow is still limited, let alone its structure that is generally assumed to be vertically uniform. In this study we extended the vertical one-dimensional model of ice shelf-ocean boundary current from Jenkins (2016) by incorporating a frazil ice module and a fairly sophisticated turbulence closure (i.e., $k-\varepsilon$ model) with the effects of density stratification. On the basis of this extended model, the study reproduced the measured thermohaline properties of a perennially-prominent supercooled ice shelf-ocean boundary current underneath the Amery Ice Shelf in East

Antarctica, and conducted extensive sensitivity runs to a wide range of factors, including advection of scalar quantities, far-field geostrophic currents, basal slope, and the distribution of frazil ice crystal size. Based on the simulation results, the following conclusions can be drawn: Firstly, it can be difficult to reasonably reproduce the vertical structure of the ice shelf-ocean boundary current using a constant eddy viscosity/diffusivity near the ice shelf base. Secondly, although there are no direct observations of the size of frazil ice crystals beneath the ice shelves, the size of the finest ice crystals that play an important role in controlling the ice shelf-ocean boundary current is strongly suggested. Lastly, but most importantly, the ice shelf-ocean boundary layer response to the vertical gradient of frazil ice concentration will significantly reduce the level of turbulence. Therefore, this study highlights the importance of the strong interaction between frazil ice formation and the hydrodynamics and thermodynamics of ice shelf-ocean boundary layer. This interaction must not only be included, but also be resolved at high resolutions in three-dimensional coupled ice shelf-ocean models applied to cold ice cavities, which will have a potential impact on the overall ice shelf mass balance and the Antarctic Bottom Water production.

Keywords: Ice shelf; Boundary current; Supercooling; Frazil ice; Stratification; Turbulence

1. Introduction

Ice shelves, which are the extensions of ice sheets over the ocean, buttress the outflow of ice from the grounded Antarctic ice sheet (Rignot et al., 2008). They lose mass primarily through iceberg calving and basal melting, with the latter in particular driving the ice shelf thinning, which is believed to be related to the loss of the Antarctic ice sheet (Pritchard et al., 2012), as well as the sea-level rise (DeConto and Pollard, 2016). The most severe basal melting usually occurs underneath the small warm-cavity ice shelves in the Bellingshausen and Amundsen Seas (Rignot et al., 2013), which is directly associated with the warming of surrounding continental shelf waters (Schmidtko et al., 2014; Cook et al., 2016). In contrast, large ice shelves make a disproportionately small contribution to net basal melting despite melt rates of over 5 m/yr on their deep grounding lines (Rignot et al., 2013); specifically, Filchner-Ronne and Amery Ice Shelves, which are the second and third largest ice shelves by area in Antarctica, respectively, gained mass during the period 1994-2012 (Paolo et al., 2015). An abundance of marine ice beneath both ice shelves (Fricker et al., 2001; Sandhäger et al., 2004; Craven et al., 2009) could account for their mass gain, which typically originates from the frazil ice-laden supercooled Ice Shelf Water (ISW) plume being sourced from the deep grounding lines (Holland et al., 2007; Galton-Fenzi et al., 2012).

Any water mass whose temperature falls below the surface freezing point can be referred to as ISW. Due to the buoyancy of the ISW in the ambient fluid, the ISW plume rises along the ice shelf base and gradually transits from being warmer than the freezing point to being in a supercooled state because of the depth-dependent freezing point when the plume approaches the ice shelf front (Lewis and Perkin, 1986). As soon as the ISW becomes supercooled, the suspended frazil ice within the plume, which has been initially seeded by broken basal dendrites, fracturing of the ice shelf, or nucleation of the suspended impurities within supercooled seawater (Jenkins and Bombosch, 1995), grows and deposits out of the plume onto the ice shelf base to form an accreted marine ice layer (Bombosch and Jenkins, 1995). Marine ice not only

makes a significant contribution to the mass balance of the Antarctic ice sheet, for example, contributing 5% and 9% of the total volume of Filchner-Ronne (Sandhäger et al., 2004) and Amery (Fricker et al., 2001) Ice Shelves, respectively, but also heals rifts, thereby stabilizing the ice shelf (Glasser et al., 2009; Holland et al., 2009). Furthermore, the supercooled ISW plume flowing out from beneath the ice shelves not only influences the adjacent sea ice ecosystem processes (Smetacek et al., 1992), but also controls the properties and volume of Antarctic Bottom Water (Foldvik et al., 2004; Matsumura and Hasumi, 2010; Williams et al., 2016). This has been a vital issue to the global climate system and biogeochemical cycles (Orsi et al., 1999; Johnson, 2008; Marshall and Speer, 2012). Therefore, it is of utmost significance to better understand the structure and dynamics of the supercooled ice shelf-ocean boundary current, combined with the associated interior frazil ice processes.

2. Motivation

Recent reviews present achievements related to Antarctic ice shelf-ocean interactions to date, with emphasis on modeling or parameterizing, and observationally monitoring these interactions and associated influences on the surrounding waters (Asay-Davis et al., 2017; Dinniman et al. 2016; Silvano et al., 2016). However, knowledge of frazil ice-laden supercooled ice shelf-ocean boundary currents is one of the least known issues to the community. The ice shelf-ocean boundary current is analogous to a dense current on a seabed slope (e.g., overflows from marginal seas), which has a velocity maximum somewhere below ice shelf base and reversed shear below, and the current relaxes to the far-filed flow. Within that current, we refer to the boundary frictionally influenced part as the “boundary layer” beyond which is purely geostrophic (Jenkins, 2016).

The process of these flows can be described using the plume theory, which was first applied by MacAyeal (1985). All the properties of the ISW plume are assumed to be well-mixed, and are represented as depth-averaged quantities in this framework (Jenkins, 1991). The well-mixed temperature and salinity of the supercooled ISW have been verified by borehole observations under the Ronne (Nicholls and Jenkins,

1993) and Amery Ice Shelves (Herraiz-Borreguero et al., 2013). However, the vertical profiles of frazil ice concentration (FIC) and oceanic velocity may not to be uniform in the vertical direction, despite the complete lack of corresponding measurements.

The FIC profile can hardly be vertically uniform due to the counteraction between the upward crystal buoyancy and downward turbulent diffusion, which leads to a nonlinear decrease in FIC with depth from the ice shelf or sea ice base, and thus the resultant stable stratification. That has been confirmed by some idealized one-dimensional simulations (Omstedt and Svensson, 1984; Omstedt, 1985; Holland and Feltham, 2005; Heorton et al., 2017). By drawing on the dynamical analogy with suspended sediment (Cheng et al., 2013; 2016), Cheng et al. (2017) introduced an expression for the equilibrium profile of FIC into an existing depth-averaged ISW plume model, and significantly improved the marine ice production beneath the western side of the Ronne Ice Shelf, as well as the sub-ice platelet layer thickness under the fast ice in McMurdo Sound (Cheng et al., 2019). Nevertheless, the equilibrium profile is essentially a first-order approximation, so the vertical dimension should be considered in the frazil ice module. It is worth mentioning that Holland and Feltham (2005) is the only work, as far as we know, that uses vertical one-dimensional model to study the frazil dynamics beneath an ice shelve. However, they did not consider the vertical structure of the ice shelf-ocean boundary current, and the salinity component was also excluded. Furthermore, they employed a constant diffusivity for simplicity, and did not consider the heat exchange at either ice shelf base or plume-ambient seawater interface.

As the vertically inverted analog to the frazil ice, ignoring for the moment thermohaline exchanges, the suspended sediment-induced stratification suppresses the turbulence, which was first detected by Vanoni (1946), and can be represented indirectly with a reduction in the von Kármán parameter, as verified experimentally (Valiani, 1988) and theoretically (Guo and Julien, 2001; Castro-Orgaz et al., 2012). This sediment-induced turbulence damping has been extensively studied through the use of a stratification-dependent eddy diffusivity, analogous to that in a stably-stratified atmospheric surface layer (Smith and McLean, 1977; Villaret and

Trowbridge, 1991; Herrmann and Madsen, 2007) and fairly sophisticated turbulence closures (Adams Jr and Weatherly 1981; Sheng and Villaret, 1989; Winterwerp, 2001, 2006; Wright and Parker, 2004; Amoudry and Souza, 2011). These extensive studies have confirmed the role of sediment-induced turbulence damping in the control of hydrodynamics of the bottom boundary layer, and thus bed erosion and deposition. Therefore, the frazil-induced stratification is hypothesized to exert considerable influences on the supercooled ice shelf-ocean boundary layer, the confirmation of which is of particular concern in this study by using a more realistic turbulence closure rather than the constant diffusivity.

Regarding the vertical structure of the ice shelf-ocean boundary current, to date, Jenkins (2016) is the exclusive work that gives a fundamental insight into this unique sub-ice shelf flow structure when basal melting occurs. The resultant meltwater formed beneath the ice is forced by its own buoyancy acting up the slope of the ice shelf base. The phase change at the ice shelf-ocean boundary makes this problem unique in the open-ocean. However, Jenkins (2016) did not discuss the effects of supercooling, and thus the influences exerted by the suspended frazil ice. If frazil ice processes are included, heat and freshwater exchanges at the crystal-seawater interface should be considered in addition to that at the ice shelf base. Besides, a constant viscosity/diffusivity was still adopted in Jenkins (2016). It is worth noting that owing to the limitation of the coarse resolution near the ice shelf base, the three-dimensional ice shelf-ocean coupled models can only roughly represent the vertical structure of this boundary current at a few grid points. In addition, there is almost no knowledge about the effects of frazil ice processes on this vertical structure beneath an ice shelf.

Therefore, the motivation of this study is to provide insight into the vertical structure of the supercooled ISW plume by virtue of a one-dimensional (normal to the ice shelf base) model, including a more realistic turbulence closure. As a complement to Jenkins (2016) that focused on the ice shelf basal melting case, this study may lead to the future observation and modeling of ice shelf-ocean interactions under supercooling condition within cold cavities.

3. Model

The model adopted here is an extension of the vertical one-dimensional buoyancy- and/or pressure gradient-forced frictional ice shelf-ocean boundary current model developed by Jenkins (2016). Comparing with Jenkins (2016), we incorporate $k-\varepsilon$ turbulence closure and frazil ice dynamics for this study. The rotated coordinate system used in the model is illustrated in Fig. 1, that is, z-normal to the ice shelf base, x-parallel to the principal slope (upslope), and y-perpendicular to the principal slope of the ice shelf base (across-slope).

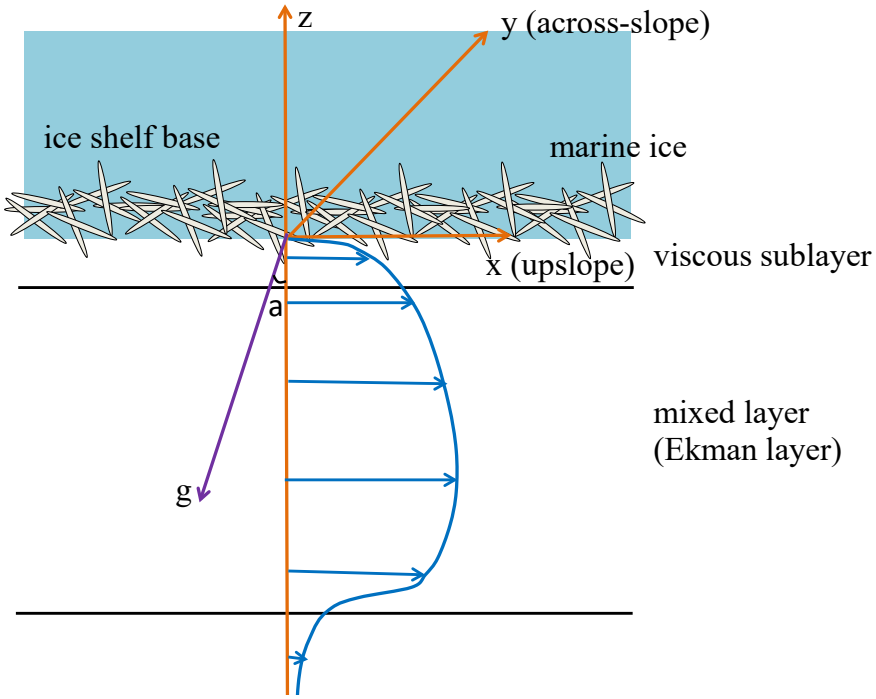

Fig. 1. Schematic of the ice shelf-ocean interface and underlying boundary current. The purple arrow denotes the direction of gravity, implicitly indicating the decreasing thickness of the ice shelf with the basal slope $\tan\alpha$ along the x direction. Blue arrows show velocity vectors for a typical upslope current profile.

3.1. Governing equations

The ISW density is assumed to be represented by a mixture of seawater and frazil ice. Then, the equation of state can then be written as:

$$\rho = \rho_0(1 - C_i)[1 + \beta_S(S - S_0) - \beta_T(T - T_0)] + \rho_i C_i \quad (1)$$

where ρ is the potential density of frazil-seawater mixture, T is the temperature, S is the salinity, $\rho_i = 920\ \mathrm{kg.m^{-3}}$ is the ice density, $\rho_0 = 1030\ \mathrm{kg.m^{-3}}$, $T_0 = -2\ ^{o}\mathrm{C}$, and $S_0 = 34.5\ \mathrm{psu}$ are the reference density of seawater, reference temperature, and reference salinity, respectively, $\beta_T = 3.87 \times 10^{-5}\ ^{o}\mathrm{C}^{-1}$ and $\beta_S = 7.86 \times 10^{-4}\ \mathrm{psu}^{-1}$ are expansion coefficients, C_i is the total volumetric FIC, which is distributed between N_i size classes, such that $C_i = \sum_{n=1}^{N_i} C_{i,n}$.

The simplified momentum equations (Eqs. (2) and (3)) are adopted from in Jenkins (2016):

$$\frac{\partial u}{\partial t} - \phi v = -g\cos\alpha \frac{\partial \eta}{\partial x} + \frac{\rho_a - \rho}{\rho_0} g \sin\alpha + \frac{\partial}{\partial z}\left(A_z \frac{\partial u}{\partial z}\right) \quad (2)$$

$$\frac{\partial v}{\partial t} + \phi u = -g\cos\alpha \frac{\partial \eta}{\partial y} + \frac{\partial}{\partial z}\left(A_z \frac{\partial v}{\partial z}\right) \quad (3)$$

where u and v are components of the current vector in the x (upslope) and y (across-slope) directions, respectively, t is the time, z is the axis normal to the ice shelf-ocean interface, ρ_a is the ambient seawater density, η is the instantaneous deviation of the ice shelf-ocean interface from its static position, A_z is the eddy viscosity that is determined by a specific turbulence closure shown later, ϕ is the Coriolis parameter, g is the acceleration of gravity, α is the angle between the ice shelf-ocean interface and the horizontal.

Following Holland and Feltham (2005), the vertical one-dimensional governing equation of FIC for each size class is given by

$$\frac{\partial C_{i,n}}{\partial t} = \frac{\partial}{\partial z}\left(K_z \frac{\partial C_{i,n}}{\partial z}\right) - w_{i,n}\cos\alpha \frac{\partial C_{i,n}}{\partial z} + N'_n + \begin{cases} F(w'_n, w'_{n+1}) & \text{for melting} \\ F(w'_{n-1}, w'_n) & \text{for freezing} \end{cases} \quad (4)$$

where K_z is the eddy diffusivity of scalars, which is assumed to be equal to A_z (i.e., Prandtl number $P_r = 1$, which eliminates the influences caused by differential scalar diffusion; Omstedt and Svensson, 1984; Omstedt, 1985; Jordan et al., 2014, 2015; Jenkins, 2016), $w_{i,n}$ is the frazil crystal rising velocity for each size class, which is estimated here by an explicit empirical function of frazil diamieter, as proposed by Morse and Richard (2009), w'_n and N'_n are the rates of frazil melting ($w'_n > 0$) or freezing ($w'_n < 0$) and frazil secondary nucleation of size class n, respectively, F is

the transfer term due to freezing (melting) of frazil ice between class n and $n-1$ $(n+1)$. The parameterizations of w'_n, N'_n, and F are well documented (Smedsrud and Jenkins, 2004; Holland and Feltham, 2005, 2006; Galton-Fenzi et al., 2012; Cheng et al., 2017), thus it is thus redundant to repeat these formulations here. However, it is worth mentioning that frazil ice size is the most important but the least constrained determinant of all the aforementioned parameterizations associated with the frazil ice processes. Accordingly, the sensitivity of the vertical structure of the ice shelf-ocean boundary current to the distribution of the frazil ice crystal size should be indispensably examined later on.

The conservation equations for T and S with the terms associated with frazil ice are

$$\frac{\partial T}{\partial t} = \frac{\partial}{\partial z}\left(K_z \frac{\partial T}{\partial z}\right) + \left(T_f - T - \frac{\mathcal{L}}{c_w}\right) w' \tag{5}$$

$$\frac{\partial S}{\partial t} = \frac{\partial}{\partial z}\left(K_z \frac{\partial S}{\partial z}\right) - S w' \tag{6}$$

where T_f is the in-situ freezing point that is dependent on salinity and pressure (Jenkins, 1991), $\mathcal{L} = 3.35 \times 10^5\ \mathrm{J.kg^{-1}}$ is the latent heat of ice fusion, $c_w = 3974\ \mathrm{J.kg^{-1}.\ ^oC^{-1}}$ is the specific heat capacity of seawater, and $w' = \sum_{n=1}^{N_i} w'_n$ is the net growth rate of frazil ice amongst full-size classes.

In order to more quantitatively characterize the turbulent mixing in the boundary current, a fairly sophisticated turbulence closure, i.e., $k-\varepsilon$ model (Rodi, 2017), is used in this study, which takes into account the effect of density stratification, compared to the frequently-used constant eddy viscosity/diffusivity. The corresponding governing equations are given as follows:

$$\frac{\partial k}{\partial t} = \frac{\partial}{\partial z}\left(\frac{A_z}{\sigma_k}\frac{\partial k}{\partial z}\right) + P_s + P_b - \varepsilon \tag{7}$$

$$\frac{\partial \varepsilon}{\partial t} = \frac{\partial}{\partial z}\left(\frac{A_z}{\sigma_\varepsilon}\frac{\partial \varepsilon}{\partial z}\right) + \frac{\varepsilon}{k}\left(c_{1\varepsilon}P_s + c_{3\varepsilon}P_b - c_{2\varepsilon}\varepsilon\right) \tag{8}$$

$$P_s = A_z\left[\left(\frac{\partial u}{\partial z}\right)^2 + \left(\frac{\partial v}{\partial z}\right)^2\right] \tag{9}$$

$$P_b = A_z \frac{g\cos\alpha}{\rho_0}\frac{\partial \rho}{\partial z} \tag{10}$$

$$A_z = c_\mu \frac{k^2}{\varepsilon} \tag{11}$$

where k is the turbulent kinetic energy, ε is its dissipation rate, P_s is the production due to shear, P_b is the production/destruction due to buoyancy, $\sigma_k = 1.4$ and $\sigma_\varepsilon = 1.3$ are the Schmidt numbers for the eddy diffusivity of turbulent kinetic energy and dissipation, respectively, $c_\mu = 0.09$, $c_{1\varepsilon} = 1.44$, $c_{2\varepsilon} = 1.92$, and $c_{3\varepsilon} = 0.8$ are constants. All of the governing equations listed above are discretized in finite-difference form, and the Coriolis force is treated using a semi-implicit approach (see Kämpf, 2010 for details). Moreover, the modeled boundary current thickness (i.e., the vertical model domain) is set to 200 m. The vertical grid spacing and time step are set to 1 m and 0.25 s, respectively.

3.2. Boundary conditions

The thickness of the viscous sublayer that adheres to the solid boundary is typically of the order of centimeters (Soulsby, 1983), which is comparable to the scales of the basal roughness forms (Owen and Thomson, 1963; Yaglom and Kader, 1974). Accordingly, the interactions between the flow and ice shelf basal roughness forms, involving thermohaline mixing and momentum transfer, within this thin layer can only be fully resolved by large-eddy simulations (Vreugdenhil and Taylor, 2019) or direct numerical simulations (Mondal et al., 2019) with the vertical grid resolution of the order of millimeters or even finer. Because such small-scale processes cannot be resolved under the relatively much coarser grid resolution (on the order of meters) used in this study, it is necessary to use the approach of the log-law of the wall to parameterize the unresolved flow. In this approach, the first grid point (denoted by the subscript "1") is placed outside of the viscous sublayer and below the roughness elements. The resultant interfacial shear stress τ_0 is related to the flow speed at the first grid point $|U_1| = \sqrt{(u_1{}^2 + v_1{}^2)}$ by the drag coefficient C_d, as follows:

$$\tau_0 = \rho u_*{}^2 = \rho A_{z0} \frac{|U_b - U_1|}{\Delta z} = \rho A_{z0} \frac{|U_1|}{\Delta z} \tag{12a}$$

where Δz is the vertical grid spacing, the velocity U_b at the ice shelf base is set to zero, $u_* = \sqrt{A_{z0} \frac{|U_1|}{\Delta z}}$ is the friction velocity in which the near-base value A_{z0} at the first time step can be set by an initial value, e.g., a specified minimum value $A_{z,\min}$.

Alternatively, the basal shear stress can also be parameterized using a quadratic drag law formulated as:

$$\tau_0 = \rho u_*^2 = \rho\left(\sqrt{C_d}|U_1|\right)^2 \tag{12b}$$

The drag coefficient C_d is derived from the log law with a specified surface roughness length of z_0:

$$\sqrt{C_d} = \frac{\kappa}{\ln(\Delta z/z_0)} \tag{13}$$

where $\kappa = 0.4$ is the von Kármán constant. According to Robinson et al. (2017), the ice shelf base with accreted marine ice could be regarded as a very rough interface. Thus, following Cebeci and Bradshaw (1977), z_0 can be specified by

$$z_0 = k_s/30 \tag{14}$$

where k_s is the equivalent height of the basal roughness forms. Eq. (12a) equaling Eq. (12b) leads to the following expression to calculate A_{z0} for the new value of u_* at the next time step:

$$A_{z0} = u_*\sqrt{C_d}\Delta z \tag{15}$$

In addition, the zero values of the turbulent kinetic energy k and the dissipation rate ε at the ice shelf base are specified as a result of the dominant role played by the molecular viscous forces over the shear-generated turbulence within the viscous sublayer.

The upper boundary (UB) conditions for T and S are established by three-equation formulations (Holland and Jenkins, 1999):

$$c_w\gamma_T(T_{UB} - T_b) = m'\mathcal{L} + m'c_i(T_b - T_i) \tag{16}$$

$$\gamma_S(S_{UB} - S_b) = m'S_b \tag{17}$$

$$T_b = aS_b + b - cB \tag{18}$$

where m' is the basal melt ($m' > 0$)/freeze ($m' < 0$, which is the major situation in this study) rate, $c_i = 2009\ \mathrm{J.kg^{-1}.\ ^oC^{-1}}$ is the specific heat capacity of ice, T_i is the internal ice shelf temperature, T_b and S_b are the basal temperature and salinity, respectively, T_{UB} and S_{UB} are essentially located on the upper edge of the outer turbulent region (the upper solid black line in Fig. 1), γ_T and γ_S are the thermal and haline exchange velocity, respectively, which can be determined by Eqs. (14-18) in

Holland and Jenkins (1999), B is the local ice shelf draft relative to the mean sea level, $a = -0.0573\ ^{o}C.psu^{-1}$, $b = 0.0832\ ^{o}C$, and $c = -7.61 \times 10^{-4}\ ^{o}C.m^{-1}$ are constants. The third term in Eq. (16) can be omitted in the case of basal freezing (Holland and Jenkins, 1999). Eqs. (16-18) are combined to solve for m', T_b, and S_b, and then the UB flux conditions for T and S can then be specified by

$$K_z \frac{\partial T}{\partial z}\bigg|_{UB} = \gamma_T (T_{UB} - T_b);\ K_z \frac{\partial S}{\partial z}\bigg|_{UB} = \gamma_S (S_{UB} - S_b) \tag{19}$$

It is worth mentioning that, as shown later, we essentially focus on the situation of a relatively strong ISW plume with a prominent turbulently-mixed layer under the mildly sloping ice face. In that case, the viscous sublayer is shear-controlled, rather than convection-controlled, and is significantly compressed by the fully-developed turbulence of the outer layer (McConnochie and Kerr, 2018; Mondal et al., 2019). Therefore, both the molecular and turbulent contributions to γ_T and γ_S are included (Holland and Jenkins, 1999). Furthermore, from a conservation perspective, Eq. (19) means that the vertical thermohaline fluxes through the thin viscous sublayer adjacent to the ice shelf base are assumed to be predominantly sourced from the vertical turbulent diffusion on the uppermost side of the turbulent domain. However, as suggested by Gwyther et al. (2020), how to bridge the thermohaline fluxes across the unresolved viscous sublayer to the vertical turbulence closure in the resolved part of upper water column in a more physically-based way than here will need to be addressed with the aid of well-designed observations (McConnochie and Kerr, 2018) and high-resolution modeling (e.g., large-eddy simulations (Vreugdenhil and Taylor, 2019) or direct numerical simulations (Mondal et al., 2019)).

The UB flux condition for FIC of each class can be formulated as:

$$K_z \frac{\partial C_{i,n}}{\partial z}\bigg|_{UB} - w_{i,n} C_{i,n}\bigg|_{UB} = p'_n \tag{20}$$

where p'_n is the frazil precipitation rate for the size class n. We follow McCave and Swift (1976) in the parameterization of p'_n in terms of the product of the rising frazil ice flux and the basal shear relative to the critical shear for precipitation, which has been often referenced in the literature (Jenkins and Bombosch, 1995; Smedsrud and Jenkins, 2004; Holland and Feltham, 2005, 2006; Hughes et al., 2014; Cheng et al.,

2017, 2019).

The lower boundary (LB) conditions are specified as follows:

$$u_{LB} = u_g;\ v_{LB} = v_g \tag{21}$$

$$\left.\frac{\partial k}{\partial z}\right|_{LB} = 0;\ \left.\frac{\partial \varepsilon}{\partial z}\right|_{LB} = 0 \tag{22}$$

$$T_{LB} = T_a;\ S_{LB} = S_a \tag{23}$$

$$\left.\left(K_z \frac{\partial C_{i,n}}{\partial z} - w_{i,n} C_{i,n}\right)\right|_{LB} = 0 \tag{24}$$

where $u_g = -\frac{g\cos\alpha}{\phi}\frac{\partial \eta}{\partial y}$ and $v_g = \frac{g\cos\alpha}{\phi}\frac{\partial \eta}{\partial x}$ are the far-field upslope and across-slope geostrophic currents, respectively, T_a and S_a are the ambient seawater temperature and salinity, respectively.

4. Reference run

4.1. Model set up

The majority of hydrographic observations beneath the ice shelves correspond to higher (Stanton et al., 2013; Kimura et al., 2015) or lower (Gilmour, 1979; Jacobs et al., 1979; Nicholls et al., 1997, 2012; Robinson et al., 2010; Hattermann et al., 2012; Arzeno et al., 2014; Begeman et al., 2018) basal melt rates. In contrast, the sub-ice shelf observations associated with the prominently supercooled condition, to our knowledge, are rather sparse thus far (Nicholls and Jenkins, 1993; Herraiz-Borreguero et al., 2013). Here, in view of the perennially prominent supercooled ISW overlain by a nearby 203 m thick accreted marine ice, we use the Conductivity-Temperature-Depth (CTD) data from the borehole site AM01 underneath the Amery Ice Shelf during the austral summer in 2002 (Herraiz-Borreguero et al., 2013) to validate our Reference run (hereinafter referred to as Ref). Seven full-depth (~363 m) continuously-sampled profiles were collected from the AM01 site within the space of 4 days, showing the inherent high variability that can be attributed to vertical (e.g., internal waves) and/or horizontal (e.g., advection by tides or currents) displacements of the water column (see Fig. 2 in Herraiz-Borreguero et al., 2013). The most prominent feature of these CTD profiles is

the presence of an approximately 60 m thick ISW mixed layer (Fig. 2a and b).

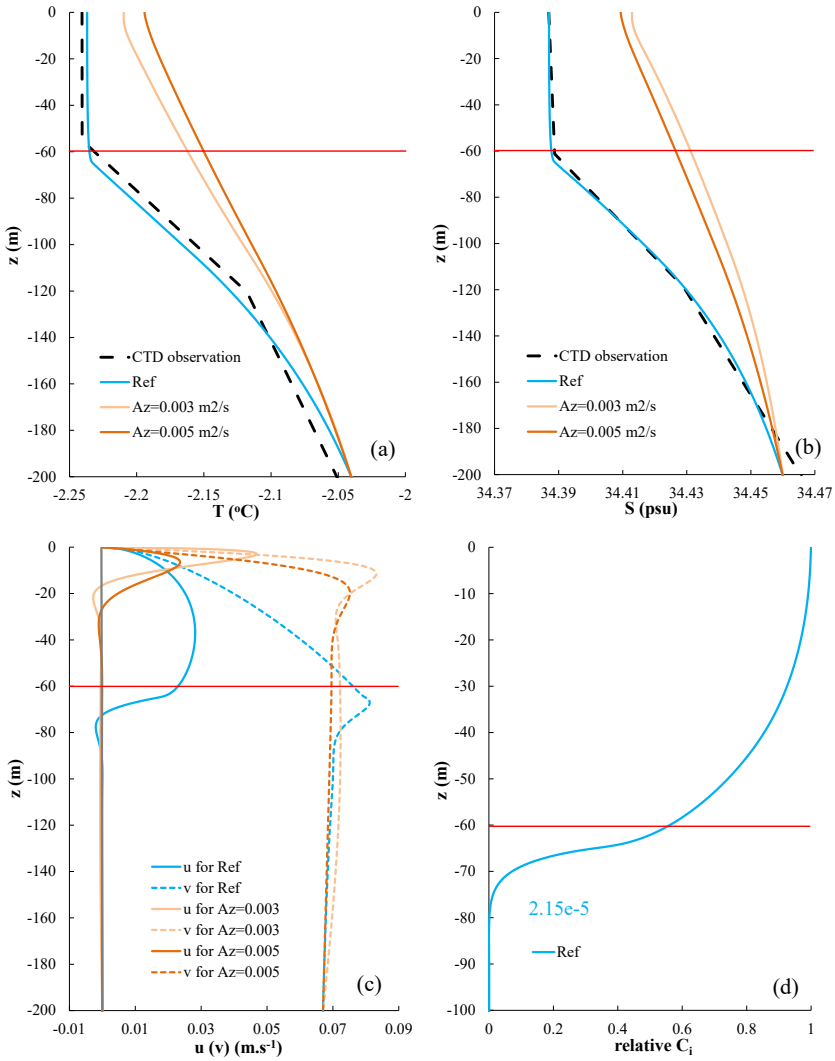

Fig. 2. Calculated vertical profiles of (a) temperature, (b) salinity, (c) velocity, and (d) total FIC relative to the value at the UB (denoted by number) in Ref and runs of different constants of viscosity ($A_z = 0.003$ and $0.005\ m^2.s^{-1}$). The ensemble-averaged CTD profiles of T and S at AM01 under the Amery Ice Shelf (Herraiz-Borreguero et al., 2013) are indicated by thick black dashed lines in (a and b), respectively. The grey solid line in (c) indicates the zero-velocity. Note that the different vertical scale is used in (d), and the depth of 60 m is delineated for comparison.

Our model domain lies between the ambient seawater and Amery Ice Shelf with

$B = -427$ m (Herraiz-Borreguero et al., 2013). The basal slope J at AM01 is set to 1.4×10^{-3} under the assumption of a linear decrease in ice shelf draft from AM01 (-427 m) to the calving front (~-287 m) within 100 km (Galton-Fenzi et al., 2012). From Jenkins (2016), the upslope density current is forced by an inclined surface for buoyancy and/or an upslope background pressure gradient, which can be represented by the far-field across-slope geostrophic current, based on the geostrophic balance. Considering the probably weak buoyant forcing owing to the roughly estimated mild slope, we specify $u_g = 0\ \mathrm{m.s^{-1}}$ and $v_g = 0.067\ \mathrm{m.s^{-1}}$ to create a relatively strong upslope boundary current, thereby having a conspicuous mixed layer. The hydrographic data at AM01 provides the ambient seawater temperature $T_a = -2.04\ ^{o}\mathrm{C}$ and salinity $S_a = 34.46$ psu.

Initial conditions are set to zero velocity, $k = 1 \times 10^{-9}\ \mathrm{m^2.s^{-2}}$, and $\varepsilon = 1 \times 10^{-13}\ \mathrm{m^2.s^{-3}}$. We specify the initial temperature $T_{ini} = -2.3\ ^{o}\mathrm{C}$ and salinity $S_{ini} = 34.42$ psu in the entire model domain. Subsequently, based on the linearized pressure freezing temperature relation, the values of the initial supercooling at UB ($T_{sc}^{ini}\big|_{UB} = -0.091\ ^{o}\mathrm{C}$) and the corresponding initial thickness of the supercooled layer ($D_{sc} = 120$ m) can be calculated by

$$T_{sc}^{ini}\big|_{UB} = T_{ini} - aS_{ini} - b + cB \tag{25}$$

$$D_{sc} = B - \frac{aS_{ini} + b - T_{ini}}{c} \tag{26}$$

However, it is worth mentioning that this choice of initial supercooling conditions has little effect on the final quasi-steady state. All runs are integrated for 50 days, sufficient to achieve the quasi-steady state.

To achieve a steady-state solution, Jenkins (2016) imposed a constant thermal driving (local temperature minus in-situ freezing point) gradient parallel to the ice-ocean interface over the entire vertical column, so that an advection effect of the boundary current can lead to a divergence in the heat flux; otherwise, the system will continuously evolve until the thermal driving is linearly-distributed normal to the interface. In our model configuration, the initial supercooling will be exhausted by the

combination of the release of latent heat due to the frazil ice growth and thermal mixing from the domain base, and will turn to the melting case that Jenkins (2016) focused on, if we take no account of the cooling advection ($u\frac{\partial T}{\partial x} > 0$). To this end, we introduce a temporospatial constant along-slope gradient of $\frac{\partial T}{\partial x}$, like Jenkins (2016), for the promotion of supercooling, and seed for each frazil ice size class in the same manner ($u\frac{\partial C_{i,n}}{\partial x} < 0$). By introducing advective cooling and seeding into the system, a balance can be reached between excess supercooling and latent heat liberated by the seeded frazil ice growth. Constrained by the observational temperature and thickness of upper mixed layer, we finally specify $\frac{\partial T}{\partial x} = 3.1 \times 10^{-6}\ {}^{o}\mathrm{C.m^{-1}}$ and $\frac{\partial C_{i,n}}{\partial x} = -4 \times 10^{-9}\ \mathrm{m^{-1}}$ by iterative model tuning. Besides being cooled, the mixed layer can also be freshened ($u\frac{\partial S}{\partial x} > 0$) by virtue of the advective ventilation of ISW from upstream. By matching with the observational salinity profile of the upper mixed layer, we also specify $\frac{\partial S}{\partial x} = 1.8 \times 10^{-6}\ \mathrm{psu.m^{-1}}$ by repeated tuning process. All the values adopted for other parameters are summarized in Table 1.

4.2. Results

The ensemble-averaged measured T and S profiles at AM01 within our model domain are depicted in Fig. 2a and b, respectively, both of which typically exhibit a three-layered structure: an approximately 60 m thick mixed surface layer, and two layers separated at the depth of about 120 m by the break point of the linear gradients in T and S, among which the middle water column has the strongest gradients. It is noteworthy that we only consider the upper 200 m thick part of the full-depth CTD profiles, because it seems to be unrealistic to model comprehensive oceanic processes over the entire distance from the ice shelf base to the bottom using a vertical one-dimensional model of boundary current.

The layered structural feature below the surface mixed layer can be approximately reproduced by adding a simplified convection terms for the scalar quantities (i.e., $w\frac{\partial X}{\partial z}$ where X represents T, S, or FIC, w is the constant vertical

velocity) to the lower half of the model system. By reducing the mismatch between the simulated and observed T and S profiles below the mixed layer, we specify $w = 3 \times 10^{-5}\ \mathrm{m.s^{-1}}$, and finally the results of Ref in the quasi-steady state are established, as shown by the blue lines in Fig. 2. We have to admit that the simplified treatment on the scalar convection, as well as scalar advection, is an inevitable limitation of our vertical one-dimensional model configuration. That, however, would be substantially improved by using a vertical two-dimensional nonhydrostatic model that is left for a later study. Nevertheless, as stated in Jenkins (2016), the contribution of the adopted small vertical velocity that is three orders of magnitude smaller than u and v (Fig. 2c) to the mass balance can be ignored.

As shown in Fig. 2c and d, the velocity and FIC profiles in the upper water column are nonuniform, contradicting the "uniform assumption". It is worth mentioning that the reason why a relative FIC (to the value at the UB) is chosen to plot its vertical profile is to discernibly present the profile pattern for comparison (as shown later), regardless of the magnitude of the FIC. The upslope and across-slope velocities increase with the distance from the ice shelf base first, and then decrease to their far-field values. Considerable shear (turbulence) is produced within the upper Ekman layer (mixed layer) near the ice shelf base, and the upslope current is purely ageostrophic, which is dominated by the balance between the Coriolis and frictional forces. In contrast, the exterior (deeper) geostrophic flow is dominated by the balance between the Coriolis force and pressure gradient and/or buoyant forcing (Jenkins, 2016). Bearing in mind the primary counteraction between the upward crystal buoyancy and the downward turbulent diffusion, the FIC profile has a positive vertical gradient that decreases towards the ice shelf base due to the increasingly strong turbulence near the ice shelf base.

Quantitative compliance with the CTD profiles verifies that our vertical one-dimensional model has the ability to reproduce the vertical thermohaline structure of the supercooled ISW plume beneath an ice shelf. Due to the complete lack of observations of the boundary current and the frazil ice within it, we cannot validate the velocity and FIC profiles here. Nevertheless, we argue that the simulated profiles

of water properties (temperature and salinity), velocity, and FIC are of certain reliability, and are inherently mutually influenced. Specifically, first of all, the advection by the boundary flow plays an important role in determining the water properties of the mixed layer, and as demonstrated later, the mixed layer thickness is critically determined by the vertical gradient of FIC. Secondly, both water properties and FIC determine the buoyancy forcing of the boundary current, and the shear-controlled turbulence is also influenced by stratification (Eqs. (7), (8), and (10)). Finally, advection also controls the FIC magnitude, the key to the suspension of frazil ice lies in the vertical turbulent diffusivity, and the thermal driving predominantly regulates the growth of frazil ice. Therefore, the vertical structure of each component should be consistent with the others. It seems to be expected that the vertical profiles of velocity and FIC are unlikely to deviate considerably from the real ones, except for other processes that have not been sufficiently resolved (e.g., more complicated vertical displacements of the water column associated with nonhydrostatic pressure) and/or are discarded (e.g., all the terms, apart from the advection of scalar quantities for ISW replenishment and frazil ice seeding, involving the gradients of ocean properties parallel to the ice-water base) in our reduced one-dimensional model become important, and/or the specific parameterizations adopted here will no longer be applicable. However, this remains for further study with a strong reliance on enriching the observational evidence for the ice shelf-ocean boundary currents, especially for their velocity and FIC.

Fig. 3 shows the time series of supercooling at UB ($T_{sc}|_{UB}$), depth-averaged C_i, and current speed $|U| = \sqrt{(u^2 + v^2)}$ at z=10 m. We find that the frazil ice-laden, supercooled ice shelf-ocean boundary current in Ref approaches a quasi-steady state after about 28 days. It is interesting to note that the FIC increases rapidly at the beginning of the simulation, which can be regarded as a "frazil-ice explosion" of the kind observed in Hanley and Tsang (1984) and simulated in Rees Jones and Wells (2018). After the establishment of Ref, it is of particular importance to examine how this benchmark responds to the variations in a wide variety of influential factors

including advection of scalar quantities, far-field geostrophic currents, basal slope, and the distribution of frazil ice crystal size, with all other parameters held at their values in Ref. Before that we first examine the influences of turbulence closure in the following section.

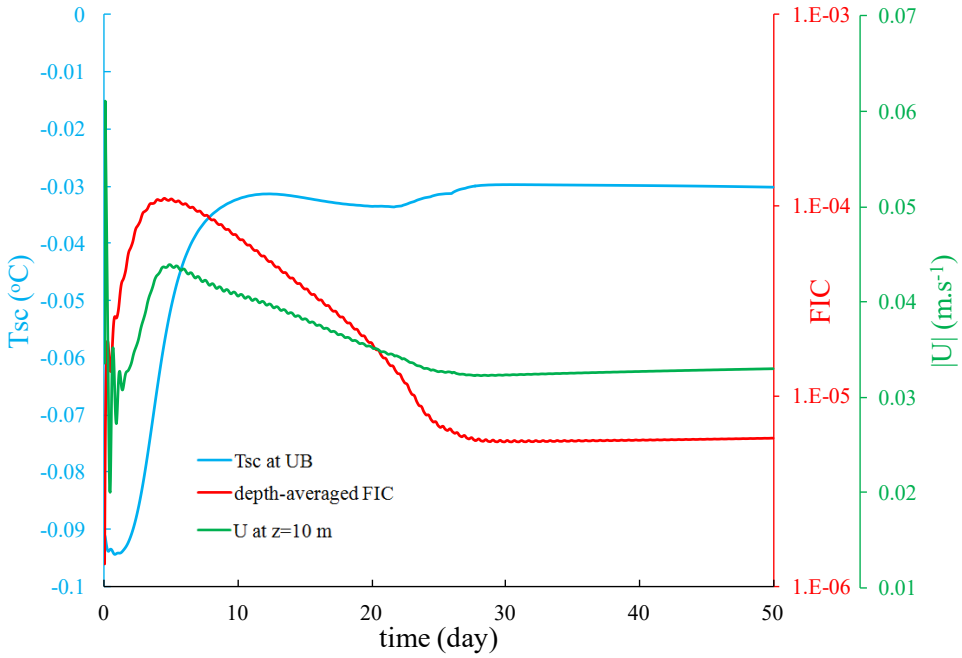

Fig. 3. Time series of supercooling at UB ($T_{sc}|_{UB}$), depth-averaged C_i, and current speed $|U|$ at z=10 m. Note that the logarithmic scale is used for depth-averaged C_i.

5. Effects of the turbulence closure

Constant eddy viscosity/diffusivity has been conventionally adopted in quite a few frazil ice-related studies (Smedsrud, 2002; Holland and Feltham, 2005; Jordan et al., 2014, 2015; Heorton et al., 2017). The calculated results corresponding to $A_z = 0.003$ and $0.005\ m^2.s^{-1}$ are shown in Fig. 2 for comparison with Ref. There is a remarkable diminution of the boundary layer thickness with constant A_z, despite being somewhat thicker with larger A_z (Fig. 2c). The upper mixed layer almost vanishes, and the entire boundary current eventually exceeds the freezing point (Fig. 2a and b).

Therefore, it can be concluded that the use of an explicit turbulence closure enables us to resolve the upper mixed layer and represent a more realistic vertical thermohaline profiles and fluxes. Within about 68 m away from the ice shelf base, the

significant turbulent kinetic energy and its dissipation are resolved by the adopted $k-\varepsilon$ turbulence closure (Fig. 4), dominating the thermohaline fluxes and maintaining the mixed layer and the shape of thermohaline profiles. It is worth mentioning that a well-defined mixed layer underneath a melting ice shelf base can be produced by using a combined turbulence closure consisting of the mixing length scheme of McPhee (1994) and the parameterization of Pacanowski and Philander (1981) (Jenkins, 2019, personal communication). Thus, more complex $k-\varepsilon$ turbulence closure is thus expected to be capable of presenting the mixed layer when net melt occurs. In contrast, the constant A_z cannot reproduce the turbulence evolution process required to maintain the upper mixed layer, so that warmer and saltier ambient seawater can erode the upper mixed layer through the mixing process.

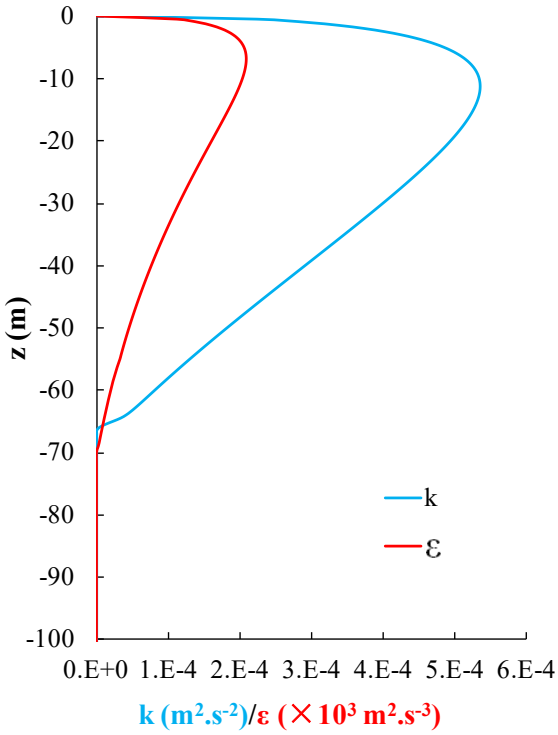

Fig. 4. Calculated vertical profiles of k and ε in Ref.

6. Sensitivity runs

6.1. Sensitivity to the external supply of FIC and ISW renewal

The sensitivity to the advective source of frazil (hereinafter referred to as ASF)

and the magnitude of the cooling and freshening (hereinafter referred to as CF) of the boundary layer are examined in Figs. 5 and 6, respectively. "0.3×ASF" and "0.75×CF" denote that the values of the upslope gradients of the FIC and thermohaline properties adopted in Ref are multiplied by 0.3 and 0.75, respectively. Obviously, the thicknesses of the upper mixed layer (defined by inflexions at the base of the mixed layer in Fig. 5a and b) and the frictionally-influenced boundary layer (defined by the depths where the positive vertical gradient of the upslope velocity reaches its maximum in Fig. 5c) decrease approximately by 33% when small amounts of frazil ice are introduced in 0.3×ASF ($\frac{\partial C_{i,n}}{\partial x} = -1.2 \times 10^{-9}\ m^{-1}$), compared with the run without frazil ice processes. It is well-acknowledged that stronger stratification leads to more suppressed turbulence generation, which can also be inferred directly from Eqs. (7), (8), and (10). From Eq. (1), larger FIC means lighter water mass. Accordingly, in view of the increase in FIC towards the ice shelf base, the supercooled ISW plume becomes more stable as the vertical gradient of FIC becomes larger. In that case, the turbulence should be further destructed due to more buoyancy gained by the production of frazil ice. As shown in Fig. 5a-c, with increasing ASF, both thicknesses of the mixed layer and the velocity boundary layer further decrease owing to further suppression of the turbulence. This is consistent with the fact that the relative FIC profile becomes more nonuniform, as shown in Fig. 5d, due to increasingly weakened downward turbulent diffusion. Here we define "nonuniformity" (NU) as a measure of the overall vertical gradient of the relative FIC, which can be described by

$$NU = \frac{1}{D_{half} C_i^{z=0}} \int_{z=-D_{half}}^{z=0} \frac{\partial C_i}{\partial z} dz = \frac{C_i^{z=0} - C_i^{z=-D_{half}}}{D_{half} C_i^{z=0}} = \frac{1}{2D_{half}} \tag{27}$$

where $z = -D_{half}$ is the depth at which FIC reaches half the value at the UB. The larger NU means the greater nonuniformity (NU monotonously increase from 0.0072 m^{-1} for 0.3×ASF to 0.0108 m^{-1} for 2.0×ASF) that indicate weaker turbulence intensity. These behaviors demonstrate that when the external source of FIC is favorable, the enhanced vertical gradient of FIC will exert a profound damping effect on the turbulence by increasing the stratification.

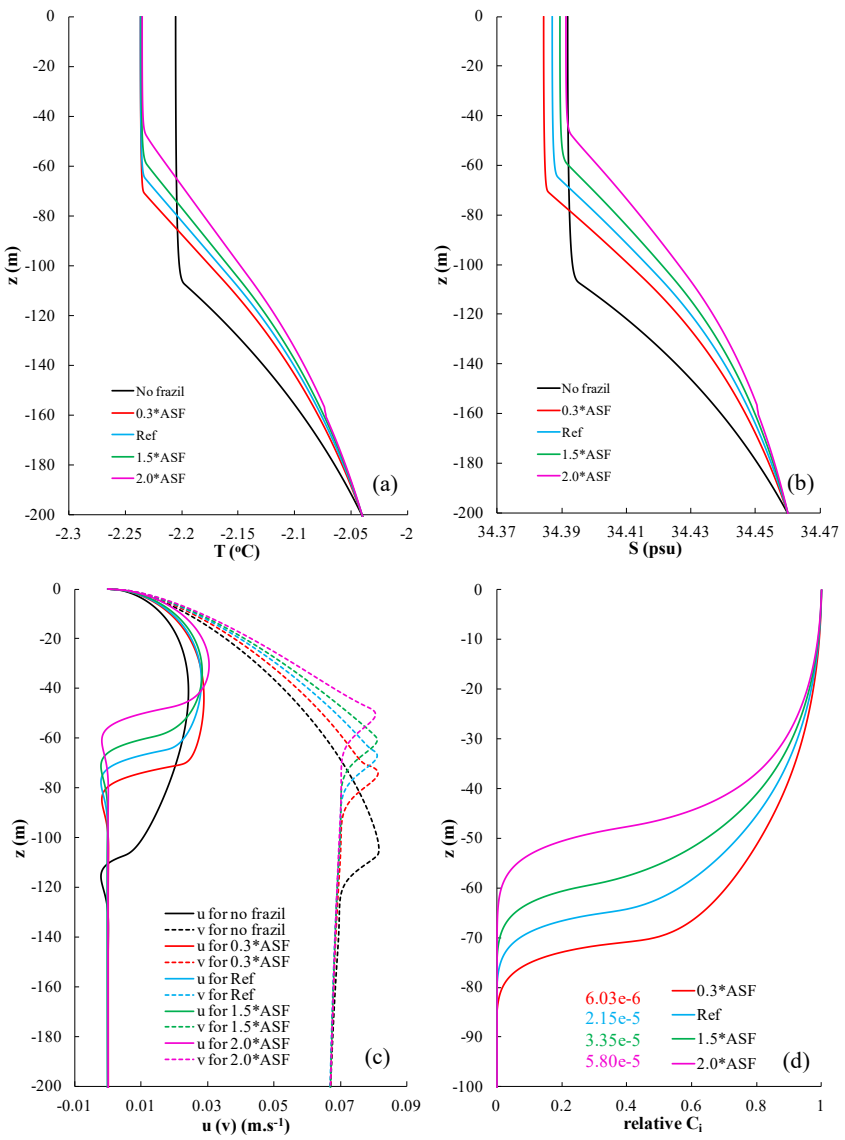

Fig. 5. As in Fig. 2, but for the sensitivity runs to advective source of FIC (ASF runs). Note that the calculated results without frazil ice processes are also plotted for comparison.

Similar behavior can also be seen in the simulated results of CF runs except for 0.75×CF (Fig. 6). The thicknesses of the mixed layer (Fig. 6a and b) and the boundary layer (Fig. 6c) increase from 0.75×CF to Ref, which corresponds to an elevated turbulence level reflected in Fig. 6d (black and blue lines). Thus, we can infer that the damping effect induced by the vertical gradient of FIC seems not to be sufficiently strong to counteract an enhancement in turbulence owing to the strengthening of buoyancy forcing by the advection of cooler and fresher water into the system.

Furthermore, it can also be inferred that the effect of a supercooling-induced FIC source on the stratification has not surpassed that of CF until in Ref. Besides ASF and CF runs, we also conduct other runs of the enhanced advection by assigning u_g to nonzero values (u_g=0 m.s^{-1} in Ref) or additionally introducing the across-slope gradient of scalar quantities to include the across-slope advection. Those model results (not shown) are also manifestation of the findings presented above yet with a distinct CF under the mixed layer when the advection is sufficiently enhanced.

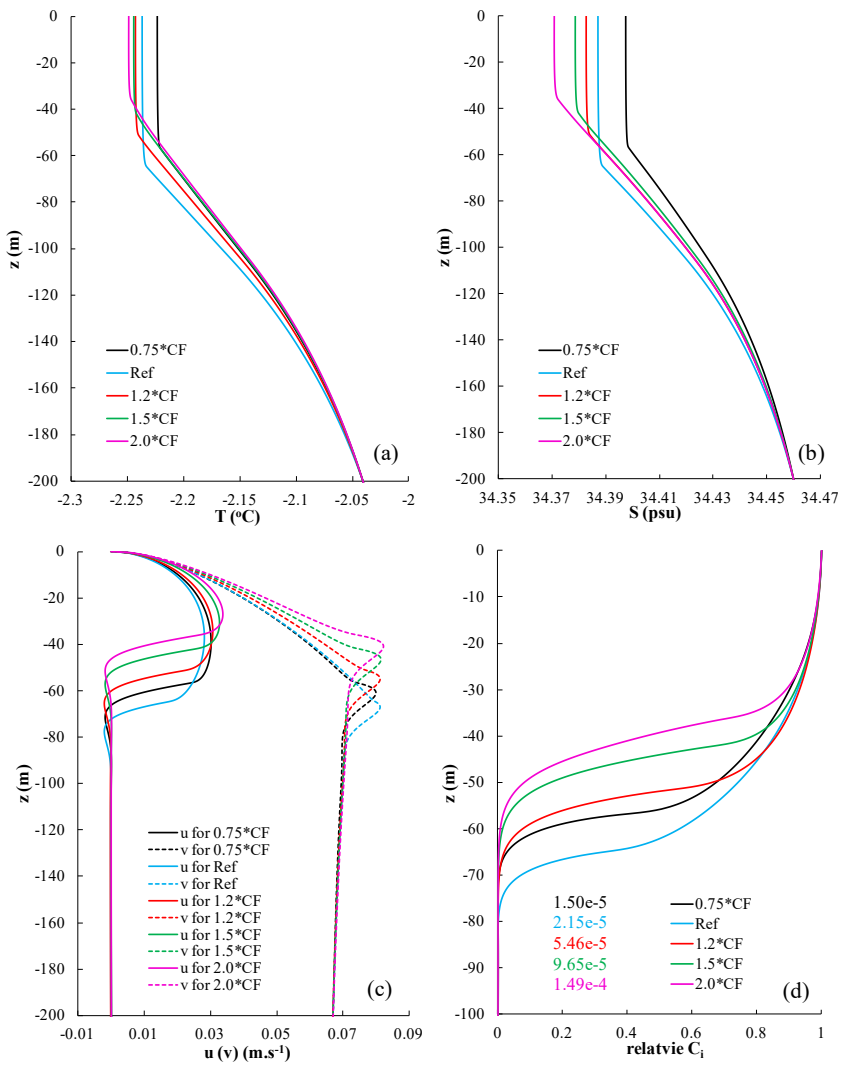

Fig. 6. As in Fig. 2, but for the sensitivity runs to advective cooling and freshening (CF runs).

6.2. Sensitivity to across-slope geostrophic current and basal slope

As shown in Fig. 7a-c, it is interesting to note that the thicknesses of the mixed layer and the boundary layer fluctuate, rather than increase monotonously, with increasing v_g. That results from the competition between the enhancement and suppression of turbulence by increasing v_g and frazil ice-induced stratification, respectively. In order to corroborate this argument, besides the mixed layer thickness, we also plot the variations of maximal A_z and NU with an increase in v_g in a normalized form (Fig. 8). As expected, the variation of maximal A_z with increasing v_g shows almost the same trend as that of mixed layer thickness, and the nonuniformity of FIC profile responds accordingly but in an inverse pattern, because larger NU corresponds to weaker turbulence as mentioned above. In addition, in order to get further insights into the effect of FIC on the turbulence, we plot the profiles of A_z and vertical gradient of the relative FIC for different v_g in Fig. 9. It is shown that the depth where the value of vertical gradient of relative FIC peaks (Fig. 9b) nearly matches the location where A_z reaches the minimum away from the ice shelf base (Fig. 9a); the latter also corresponds to the depth of the mixed layer (Fig. 7a and b).

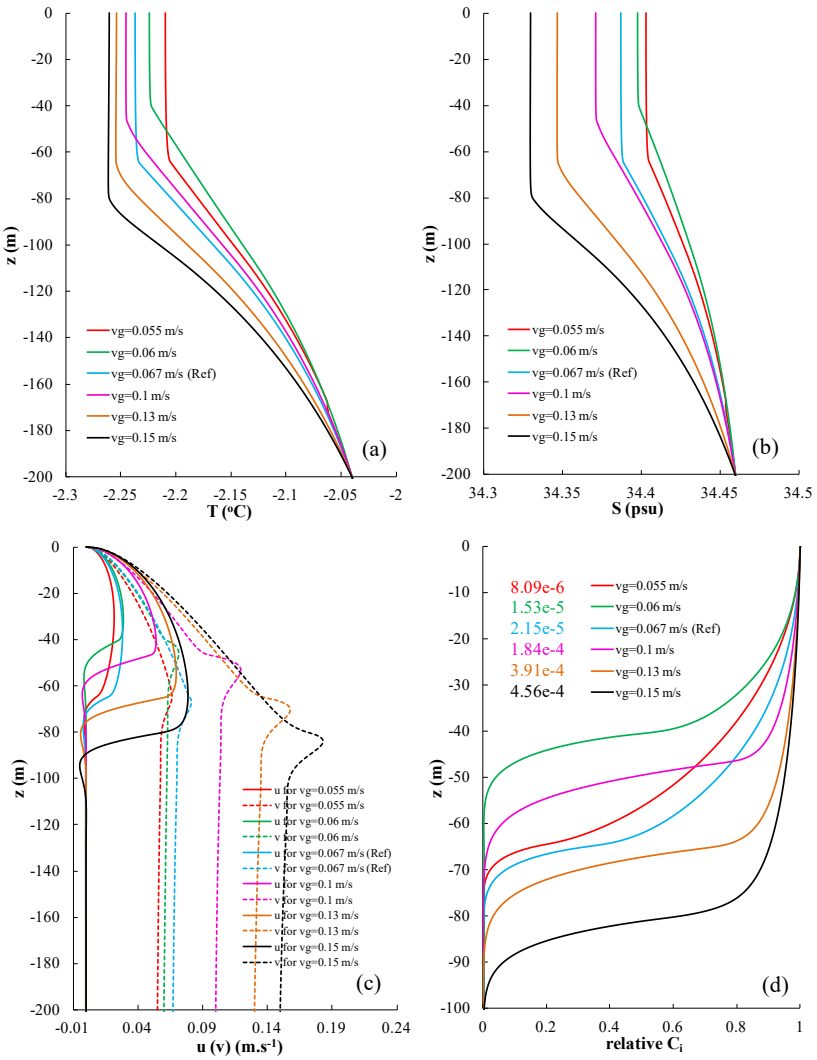

Fig. 7. As in Fig. 2, but for the sensitivity runs to across-slope geostrophic current.

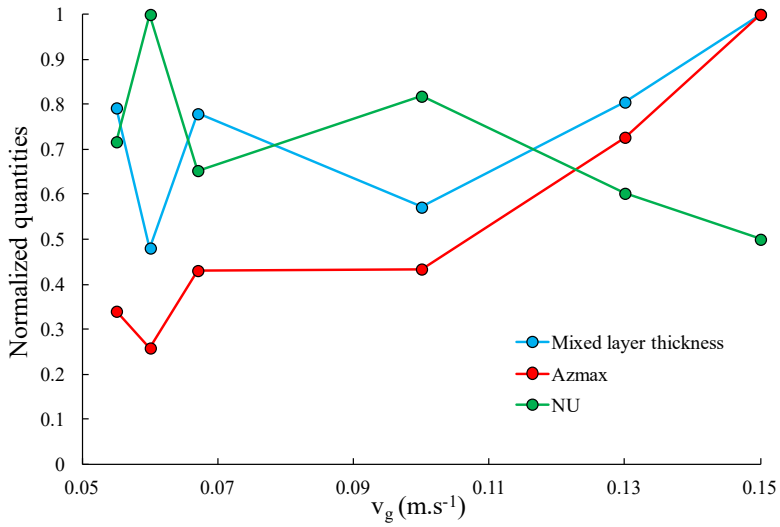

Fig. 8. Variations of the normalized mixed layer thickness, the maximal eddy viscosity/diffusivity, and NU by their corresponding maximum among all the cases of v_g with an increase in v_g.

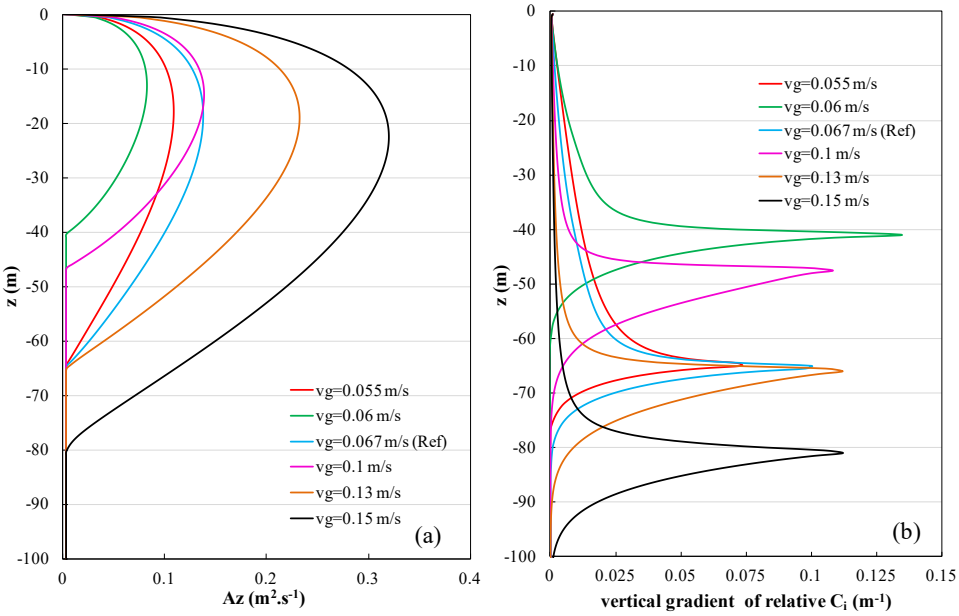

Fig. 9. Calculated vertical profiles of (a) eddy viscosity and (b) vertical gradient of the relative FIC in the sensitivity runs to across-slope geostrophic current.

So far, we can conclude that the vertical profile of FIC has a crucial influence on the vertical structure of the supercooled ice shelf-ocean boundary current by controlling the turbulence. The results of the runs with changing basal slope also exhibit similar behaviors (Figs. 10 and 11). Moreover, according to the analytical analysis of Jenkins (2016), the upslope flow is frictionally generated (i.e., purely ageostrophic) within the Ekman layer adjacent to the ice-ocean interface, and decays to zero, if u_g=0 m.s^{-1}, beyond the Ekman layer. This is consistent with our simulated results of upslope velocity. In contrast, the across-slope flow is purely geostrophic beyond the Ekman layer, which can be described by

$$-\phi v = -g\cos\alpha\frac{\partial\eta}{\partial x} + \frac{\rho_a-\rho}{\rho_0}g\sin\alpha = -\phi v_g + \frac{\rho_a-\rho}{\rho_0}g\sin\alpha \quad (28)$$

Therefore, when the basal slope becomes larger, the across-slope flow becomes stronger outside the boundary layer, which can be reflected in Fig. 10c (dashed lines).

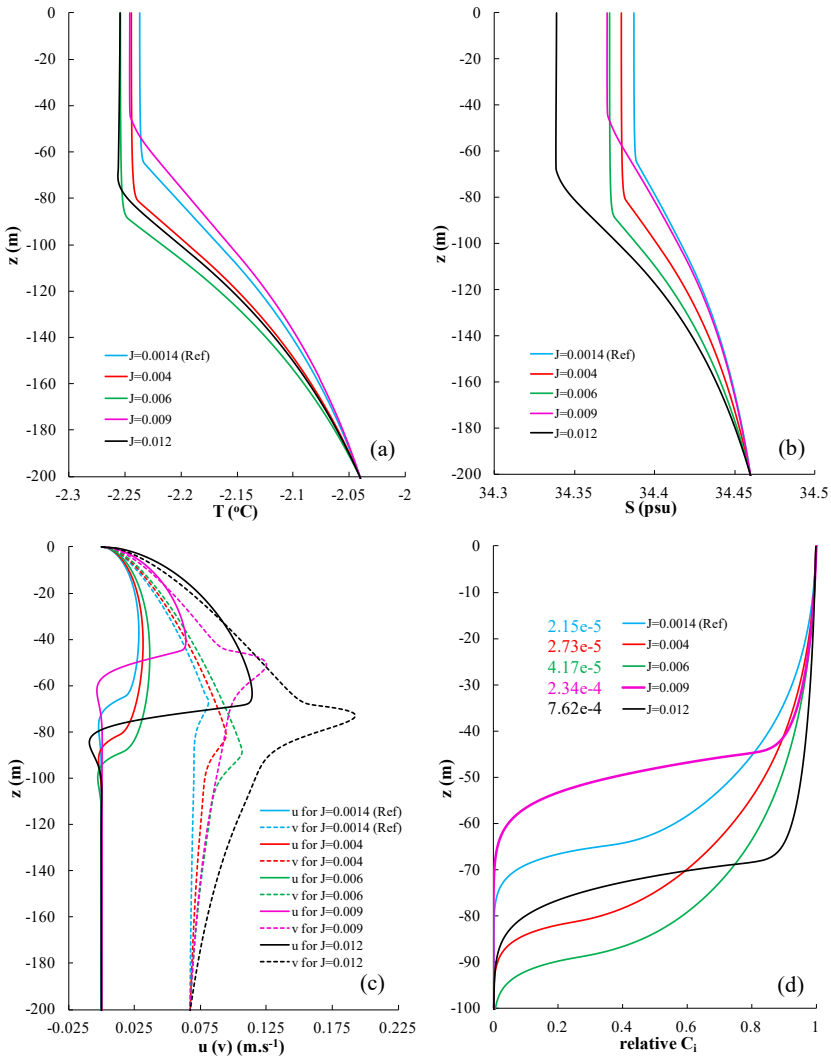

Fig. 10. As in Fig. 2, but for the sensitivity runs to ice shelf basal slope.

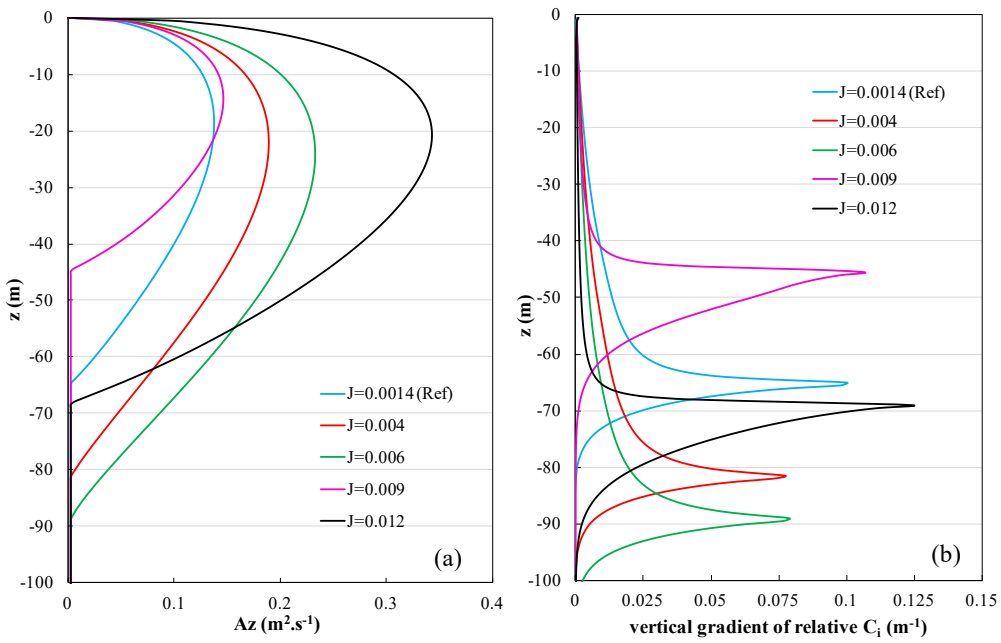

Fig. 11. As in Fig. 9, but for the sensitivity runs to ice shelf basal slope.

6.3. Sensitivity to frazil ice size

Owing to the complete lack of the observational evidence underneath an ice shelf, there has been no literature to date in guiding the least constrained parameter of frazil ice size. To this end, the distribution of frazil ice size is always set arbitrarily in the existing literature. Nevertheless, the frazil ice size, represented here by the frazil radius (see Table 1), is a critical parameter that directly determines the ice crystals growth and their rising velocity. In this study, we conduct two series of sensitivity runs to frazil ice size: in one, coarsening occurs across the full range of size classes (hereinafter referred to as CFR) by 0.1, 0.2, 0.3, 0.4, and 1 mm, in the other, coarsening occurs over a partial range (hereinafter referred to as CPR), excluding the finest class, by 0.1, 0.2, and 0.3 mm.

The simulated results of CFR and CPR are shown in Figs. 12 and 13, respectively, including the results without frazil ice processes for comparison. With regard to CFR, the thicknesses of the mixed layer (Fig. 12a and b) and the boundary layer (Fig. 12c) increase monotonically with coarsening. This also corresponds to the enhancement of turbulence (not shown) and the deepening of the location of maximum vertical gradient of FIC (Fig. 12e). This is because coarsening retards the frazil ice growth (Jenkins and Bombosch, 1995), thus the development of the vertical gradient of FIC (Fig. 12e). However, in Fig. 12d, there is a transition of the nonuniformity of the FIC profile from a decreasing trend (NU equals 0.0081, 0.0075, and 0.0073 m^{-1} for from Ref to CFR-0.2 mm) to an increasing trend (NU equals 0.0073, 0.0075, 0.0076, and 0.0085 m^{-1} for from CFR-0.2 mm to CFR-1 mm). This arises from the competition between the downward turbulent diffusion and the upward buoyant rising of frazil ice, both of which are heightened with coarsening. There is another transition for T (S) from cooling (freshening) to warming (salinizing) with coarsening. The cooling (freshening) is due to the retarding growth of frazil ice, while the warming (salinizing) results from the increased turbulent mixing with the ambient seawater as FIC diminishes. It is worth mentioning that Ref with the

relatively finest frazil size does not have the largest FIC (numbers in Fig. 12d). This is probably due to the increased upslope frazil seeding because of the extension of the boundary layer (Fig. 12c), which dominates over the retarding frazil ice growth until the coarsening of 0.3 mm. The comparatively marginal responses of mixed layer properties (Fig. 13a and b) and velocity of boundary layer (Fig. 13c) in CPR confirm an important role of the size of the finest frazil ice in governing the ISW plume properties.

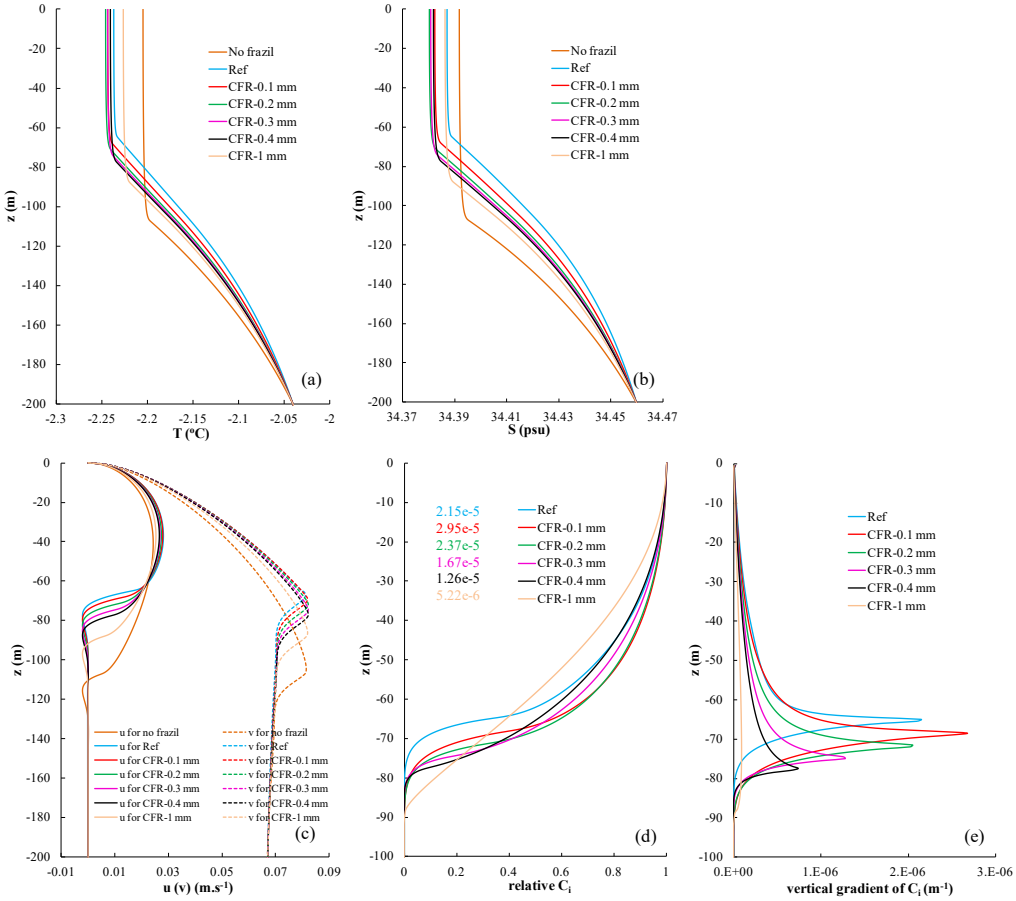

Fig. 12. As in Fig. 2, but for the CFR runs. In addition, (e) calculated vertical profiles of the vertical gradient of FIC. Note that the calculated results without frazil ice processes are also plotted for comparison.

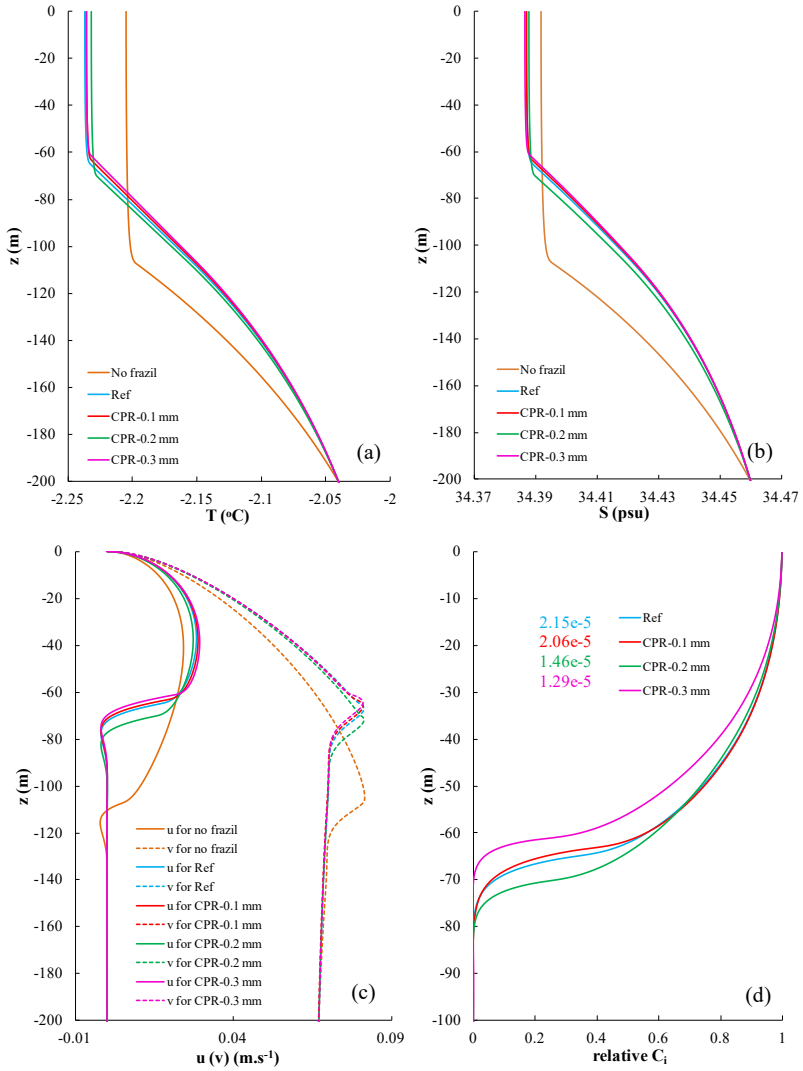

Fig. 13. As in Fig. 2, but for the CPR runs. Note that the calculated results without frazil ice processes are also plotted for comparison.

To sum up, the vertical profile of FIC plays a vital role in controlling the supercooled ice shelf-ocean boundary layer in terms of the inhibiting effect of frazil-induced stratification on the turbulence. As shown in Fig. 14, all runs indicate that the depth where the maximum vertical gradient of FIC occurs is highly consistent with the depth of the supercooled mixed layer underneath an ice shelf (the former is a bit deeper). While the investigation thus far has focused on steady forcing, for lots of ice shelves the prominent pressure gradient forcing arises from the oscillatory tides (Jenkins, 2016). To this end, based on ASF runs, we also perform the simulations

under forcing with a diurnally oscillating v_g with amplitude and time average of 0.04 and 0.067 m.s^{-1}, respectively. A general conclusion can also be drawn from the output of the last period shown in Fig. 15 that the intensity of the turbulence within the supercooled ice shelf-ocean boundary layer still depends on the vertical gradient of FIC.

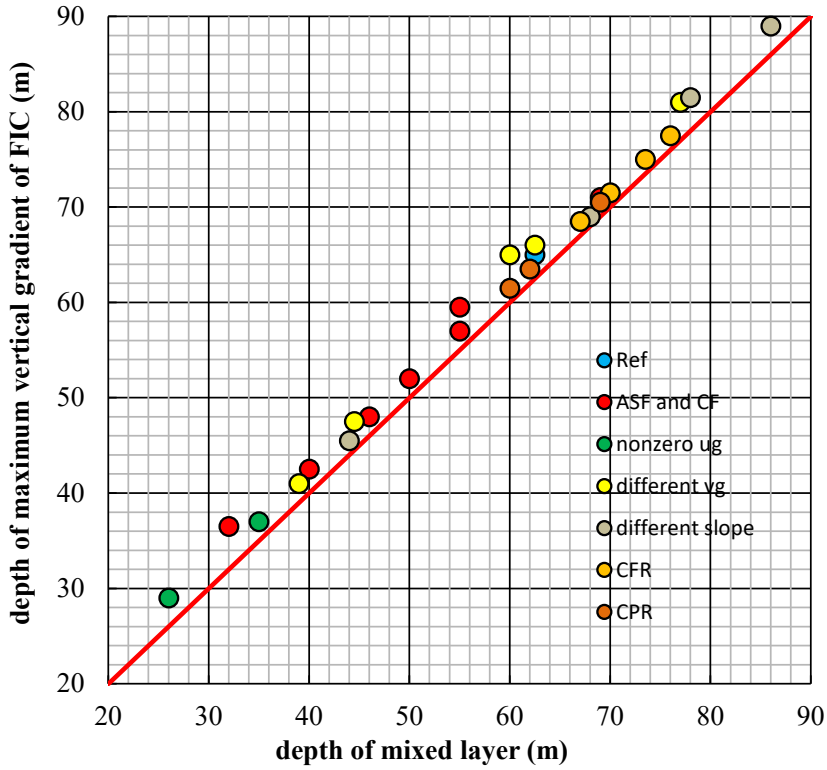

Fig. 14. Comparison between the calculated depths of the mixed layer underneath an ice shelf and the maximum vertical gradient of FIC within the ice shelf-ocean boundary layer.

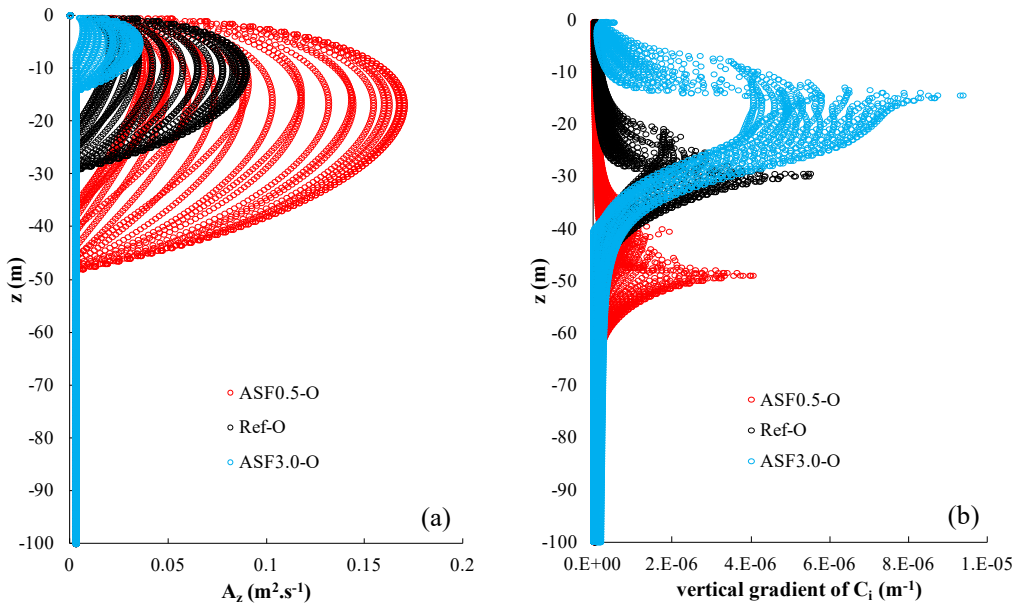

Fig. 15. Calculated vertical profiles of (a) eddy viscosity and (b) vertical gradient of FIC of the last period in the diurnal oscillation runs (denoted by O), based on the ASF runs.

7. Implications for the ice shelf-ocean coupled models

Omstedt and Svensson (1984) first emphasized the turbulence damping caused by the frazil-induced stratification in their numerical study of the initial sea-ice formation in the surface oceanic layer, and then the corresponding numerical model was validated (Omstedt, 1985) using laboratory data from Tsang and Hanley (1985). However, let alone the critical role played by FIC profile in determining the vertical structure of supercooled ice shelf-ocean boundary current, the frazil ice module has been seldom encapsulated in the existing three-dimensional ice shelf-ocean coupled models (Gwyther et al., 2015; Liu et al., 2017, 2018; Mueller et al., 2018; Naughten et al., 2019). For instance, a probably unrealistic simulated local supercooling of the ISW outflow from the western Amery Ice Shelf reaches up to -1.5 ºC (Liu et al., 2017, 2018). Given that, based on the ASF runs, we conduct three contrast runs with no frazil-induced stratification (hereinafter referred to as NFIS) taken into account in the turbulence closure. In other words, the only difference between ASF and NFIS runs is that in the later the contribution of FIC component to the stratification is ignored in

the $k-\varepsilon$ model.

It can be seen from Fig. 16c and d that as the FIC increases, the eddy viscosity calculated in the NFIS runs is amplified to some extent. Larger FIC means more buoyancy, which accelerates the boundary layer and therefore leads to stronger advective cooling (Fig. 16a) and freshening (Fig. 16b) of the mixed layer.

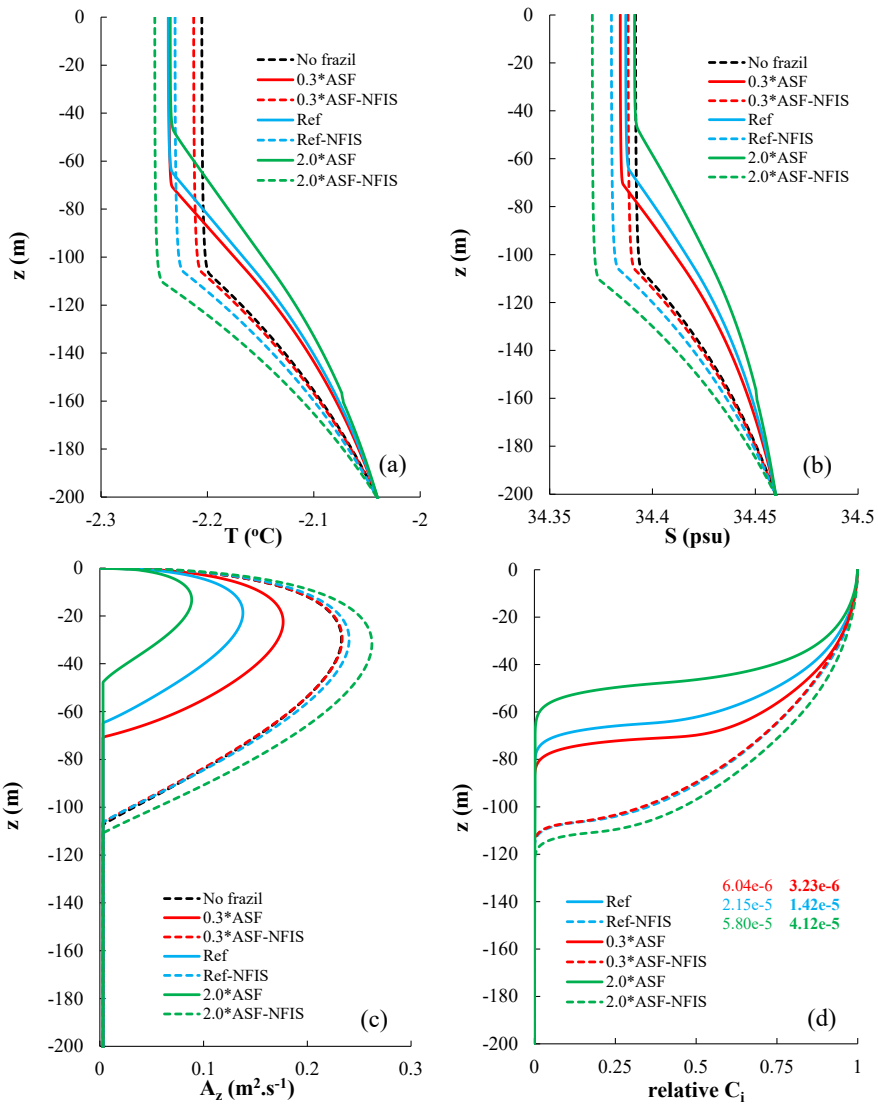

Fig. 16. Comparisons of calculated vertical profiles of (a) temperature, (b) salinity, (c) eddy viscosity, and (d) total FIC between simulations with and without (denoted by NFIS) frazil-induced stratification taken into account in turbulence closure, based on the ASF runs. In (d), the normal and bold numbers respectively denote the values of C_i at UB in the runs with and without frazil-induced stratification. Note that the calculated results without frazil ice processes are also plotted for comparison.

However, if the damping effect of frazil-induced stratification on the turbulence is included, the result is a pronounced reduction in the eddy viscosity (Fig. 16c). Therefore, as shown in Fig. 16d, a relatively high near-base FIC region is formed in 2.0×ASF when the turbulence damping is sufficiently large, which is typically analogous to the formation of a "lutocline" near the seabed in estuaries (Kirby and Parker, 1977; Wolanski, et al., 1988). Moreover, it is worth noting that the deviations of the reduced eddy viscosity from its corresponding values in NFIS runs become increasingly larger (Fig. 16c) when the turbulence damping is further reinforced by the gradually-enhanced frazil-induced stratification (Fig. 16d). Consequently, this results in the increasingly larger deviations of ISW properties within the boundary current (Fig. 16a and b), and thus leads to the potential for inaccurate evaluation of influences of ISW outflows on ambient oceanic environments. Accordingly, it is implied that resolving sufficiently the vertical profile of FIC may be indispensable for any specific turbulence closures adopted in the existing ice shelf-ocean coupled models applied to the cold ice cavities.

8. Conclusion and future works

A vertical one-dimensional model proposed by Jenkins (2016) has been extended by coupling with a frazil ice module and an explicit turbulence closure (i.e., $k-\varepsilon$ model) incorporating the effects of stratification to study the vertical structure of the supercooled ice shelf-ocean boundary current, one of the processes least studied by the Antarctic research community. The model developed in this study was used to reproduce representative profiles of measured temperature and salinity beneath several hundred meters of marine ice under the Amery Ice Shelf. This benchmark was used to extensively examine the sensitivity of the supercooled ice shelf-ocean boundary current to a variety of factors including advection of scalar quantities, far-field geostrophic currents, basal slope, and the distribution of frazil ice crystal size, which showed rather intricate responses of the ice shelf-ocean boundary current to these parameters. From these results, we can draw the following conclusions:

1. The use of a constant eddy viscosity/diffusivity cannot reasonably reproduce

the vertical structure of the ice shelf-ocean boundary current. As Jenkins (2016) argued, this simplification can only provide information about the fundamental structure of the boundary current but cannot quantitatively determine the scalar profiles underneath an ice shelf.

2. Although there are no direct observations of the size of frazil ice crystals beneath ice shelves, it is strongly suggested that the size of the finest ice crystals playing an important role in controlling the ice shelf-ocean boundary current.

3. The response of ice shelf-ocean boundary layer to the vertical gradient of FIC is to reduce appreciably the level of turbulence. This buoyant suppression of turbulence caused by frazil-induced stratification was fully accentuated in this study. In detail, the frazil-induced stratification is encapsulated in a realistic turbulence closure. The resulting eddy diffusivity in turn influences the FIC itself and other scalars (temperature and salinity), as well as hydrodynamics. Apparently, this coupling cannot be achieved by adopting a constant eddy viscosity/diffusivity, which is frequently used in the literatures. Furthermore, based on the results of all sensitivity runs, we found that the depth where the maximum vertical gradient of FIC takes place is highly consistent with the depth of the supercooled mixed layer underneath an ice shelf.

This study highlights the importance of the strong interaction between the frazil ice processes and the hydrodynamics of the ice shelf-ocean boundary current. Therefore, when applied to the cold ice cavities, three-dimensional ice shelf-ocean coupled models should not only include a frazil ice module, which is generally neglected nowadays, but also sufficiently resolve the vertical gradient of FIC for the stratification-influenced turbulence closures. This has potential consequences on the overall ice shelf mass balance and Antarctic Bottom Water production.

The vertical one-dimensional model developed here can also be used to evaluate the supercooled ISW plume underneath the sea ice adjacent to an ice shelf, with direct consequences on the sub-ice platelet layer thickness (Mahoney et al., 2011; Hughes et al., 2014; Robinson et al., 2014). However, careful adaption work needs to be done because of significant differences in the conditions under an ice shelf and sea ice

(Cheng et al., 2019). More importantly, in the near future, it is imperative that field observations of currents and FIC be carried out near the base of either ice shelves or sea ice.

Acknowledgements

We would like to thank Xylar S. Asay-Davis and Tore Hattermann for their thorough review and helpful commentaries and improvements. This work was funded by the National Natural Science Foundation of China (41941007), the Natural Science Foundation of Jiangsu Province (BK20191405), and the National Natural Science Foundation of China (41876220, 41406214).

References

Adams Jr, C. E., Weatherly, G. L., 1981. Some effects of suspended sediment stratification on an oceanic bottom boundary layer. J. Geophys. Res. Oceans 86 (C5), 4161-4172.

Amoudry, L. O., Souza, A. J., 2011. Impact of sediment-induced stratification and turbulence closures on sediment transport and morphological modelling. Cont. Shelf Res. 31 (9), 912-928.

Arzeno, I. B., Beardsley, R. C., Limeburner, R., Owens, B., Padman, L., Springer, S. R., Stewart, C. R., Williams, M. J., 2014. Ocean variability contributing to basal melt rate near the ice front of Ross Ice Shelf, Antarctica. J. Geophys. Res. Oceans 119 (7), 4214-4233.

Asay-Davis, X. S., Jourdain, N. C., Nakayama, Y., 2017. Developments in simulating and parameterizing interactions between the Southern Ocean and the Antarctic ice sheet. Curr. Clim. Change Rep. 3 (4), 316-329.

Begeman, C. B., Tulaczyk, S. M., Marsh, O. J., Mikucki, J. A., Stanton, T. P., Hodson, T. O., Siegfried, M. R., Powell, R. D., Christianson, K., King, M. A., 2018. Ocean stratification and low melt rates at the Ross Ice Shelf grounding zone. J. Geophys. Res. Oceans 123 (10), 7438-7452.

Bombosch, A., Jenkins, A., 1995. Modeling the formation and deposition of frazil ice

beneath Filchner-Ronne Ice Shelf. J. Geophys. Res. Oceans 100 (C4), 6983-6992.

Castro-Orgaz, O., Giráldez, J. V., Mateos, L., Dey, S., 2012. Is the von Kármán constant affected by sediment suspension?. J. Geophys. Res. Earth 117 (F4).

Cebeci, T., Bradshaw, P., 1977. Momentum transfer in boundary layers. Hemisphere, Washington, D.C.

Cheng, C., Song, Z. Y., Wang, Y. G., Zhang, J. S., 2013. Parameterized expressions for an improved Rouse equation. Int. J. Sediment Res. 28 (4), 523-534.

Cheng, C., Huang, H., Liu, C., Jiang, W., 2016. Challenges to the representation of suspended sediment transfer using a depth-averaged flux. Earth Surf. Proc. Land. 41 (10), 1337-1357.

Cheng, C., Wang, Z., Liu, C., Xia, R., 2017. Vertical modification on depth-integrated ice shelf water plume modeling based on an equilibrium vertical profile of suspended frazil ice concentration. J. Phys. Oceanogr. 47 (11), 2773-2792.

Cheng, C., Jenkins, A., Holland, P. R., Wang, Z., Liu, C., Xia, R., 2019. Responses of sub-ice platelet layer thickening rate and frazil-ice concentration to variations in ice-shelf water supercooling in McMurdo Sound, Antarctica. Cryosphere 13 (1), 265-280.

Craven, M., Allison, I., Fricker, H. A., Warner, R., 2009. Properties of a marine ice layer under the Amery Ice Shelf, East Antarctica. J. Glaciol. 55 (192), 717-728.

Cook, A. J., Holland, P. R., Meredith, M. P., Murray, T., Luckman, A., Vaughan, D. G., 2016. Ocean forcing of glacier retreat in the western Antarctic Peninsula. Science 353 (6296), 283-286.

DeConto, R. M., Pollard, D., 2016. Contribution of Antarctica to past and future sea-level rise. Nature 531 (7596), 591-597.

Dinniman, M. S., Asay-Davis, X. S., Galton-Fenzi, B. K., Holland, P. R., Jenkins, A., Timmermann, R., 2016. Modeling ice shelf/ocean interaction in Antarctica: A review. Oceanography 29 (4), 144-153.

Fricker, H. A., Popov, S., Allison, I., Young, N., 2001. Distribution of marine ice beneath the Amery Ice Shelf. Geophys. Res. Lett. 28 (11), 2241-2244.

Foldvik, A., Gammelsrød, T., Østerhus, S., Fahrbach, E., Rohardt, G., Schröder, M., Nicholls, K. W., Padman, L., Woodgate, R. A., 2004. Ice shelf water overflow and bottom water formation in the southern Weddell Sea. J. Geophys. Res. Oceans 109 (C2).

Galton-Fenzi, B. K., Hunter, J. R., Coleman, R., Marsland, S. J., Warner, R. C., 2012. Modeling the basal melting and marine ice accretion of the Amery Ice Shelf. J. Geophys. Res. Oceans, 117(C9).

Gilmour, A. E., 1979. Ross ice shelf sea temperatures. Science 203 (4379), 438-439.

Glasser, N. F., Kulessa, B., Luckman, A., Jansen, D., King, E. C., Sammonds, P. R., Scambos T. A., Jezek, K. C., 2009. Surface structure and stability of the Larsen C ice shelf, Antarctic Peninsula. J. Glaciol. 55 (191), 400-410.

Guo, J., Julien, P. Y., 2001. Turbulent velocity profiles in sediment-laden flows. J. Hydraul. Res. 39 (1), 11-23.

Gwyther, D. E., Galton-Fenzi, B. K., Dinniman, M. S., Roberts, J. L., Hunter, J. R., 2015. The effect of basal friction on melting and freezing in ice shelf-ocean models. Ocean Model. 95, 38-52.

Gwyther, D. E., Kusahara, K., Asay-Davis, X. S., Dinniman, M. S., Galton-Fenzi, B. K., 2020. Vertical processes and resolution impact ice shelf basal melting: A multi-model study. Ocean Model. 147, 101569.

Hanley, T. O. D., Tsang, G., 1984. Formation and properties of frazil in saline water. Cold Reg. Sci. Technol. 8 (3), 209-221.

Hattermann, T., Nøst, O. A., Lilly, J. M., Smedsrud, L. H., 2012. Two years of oceanic observations below the Fimbul Ice Shelf, Antarctica. Geophys. Res. Lett. 39 (12).

Herrmann, M. J., Madsen, O. S., 2007. Effect of stratification due to suspended sand on velocity and concentration distribution in unidirectional flows. J. Geophys. Res. Oceans 112 (C2).

Herraiz-Borreguero, L., Allison, I., Craven, M., Nicholls, K. W., Rosenberg, M. A., 2013. Ice shelf/ocean interactions under the Amery Ice Shelf: Seasonal variability and its effect on marine ice formation. J. Geophys. Res. Oceans 118

(12), 7117-7131.

Heorton, H. D., Radia, N., Feltham, D. L., 2017. A model of sea ice formation in leads and polynyas. J. Phys. Oceanogr. 47 (7), 1701-1718.

Holland, D. M., Jenkins, A., 1999. Modeling thermodynamic ice–ocean interactions at the base of an ice shelf. J. Phys. Oceanogr. 29 (8), 1787-1800.

Holland, P. R., Feltham, D. L., 2005. Frazil dynamics and precipitation in a water column with depth-dependent supercooling. J. Fluid Mech. 530, 101-124.

Holland, P. R., Feltham, D. L., 2006. The effects of rotation and ice shelf topography on frazil-laden ice shelf water plumes. J. Phys. Oceanogr. 36 (12), 2312-2327.

Holland, P. R., Feltham, D. L., Jenkins, A., 2007. Ice shelf water plume flow beneath Filchner-Ronne Ice Shelf, Antarctica. J. Geophys. Res. Oceans 112 (C5).

Holland, P. R., Corr, H. F., Vaughan, D. G., Jenkins, A., Skvarca, P., 2009. Marine ice in Larsen ice shelf. Geophys. Res. Lett. 36 (11).

Hughes, K. G., Langhorne, P. J., Leonard, G. H., Stevens, C. L., 2014. Extension of an Ice Shelf Water plume model beneath sea ice with application in McMurdo Sound, Antarctica. J. Geophys. Res. Oceans 119 (12), 8662-8687.

Jacobs, S. S., Gordon, A. L., Ardai, J. L., 1979. Circulation and melting beneath the Ross Ice Shelf. Science 203 (4379), 439-443.

Jenkins, A., 1991. A one-dimensional model of ice shelf-ocean interaction. J. Geophys. Res. Oceans 96 (C11), 20671-20677.

Jenkins, A., Bombosch, A., 1995. Modeling the effects of frazil ice crystals on the dynamics and thermodynamics of ice shelf water plumes. J. Geophys. Res. Oceans 100 (C4), 6967-6981.

Jenkins, A., 2016. A simple model of the ice shelf–ocean boundary layer and current. J. Phys. Oceanogr. 46 (6), 1785-1803.

Johnson, G. C., 2008. Quantifying Antarctic bottom water and North Atlantic deep water volumes. J. Geophys. Res. Oceans 113 (C5).

Jordan, J. R., Holland, P. R., Jenkins, A., Piggott, M. D., Kimura, S., 2014. Modeling ice-ocean interaction in ice-shelf crevasses. J. Geophys. Res. Oceans 119 (2), 995-1008.

Jordan, J. R., Kimura, S., Holland, P. R., Jenkins, A., Piggott, M. D., 2015. On the conditional frazil ice instability in seawater. J. Phys. Oceanogr. 45 (4), 1121-1138.

Kämpf, J., 2010. Advanced ocean modelling: using open-source software. Springer Science & Business Media.

Kirby, R. A., Parker, W. R., 1977. The physical characteristics and environmental significance of fine sediment suspensions in estuaries. National Academy of Sciences.

Kimura, S., Nicholls, K. W., Venables, E., 2015. Estimation of ice shelf melt rate in the presence of a thermohaline staircase. J. Phys. Oceanogr. 45 (1), 133-148.

Lewis, E. L., Perkin, R. G., 1986. Ice pumps and their rates. J. Geophys. Res. Oceans 91 (C10), 11756-11762.

Liu, C., Wang, Z., Cheng, C., Xia, R., Li, B., Xie, Z., 2017. Modeling modified circumpolar deep water intrusions onto the Prydz Bay continental shelf, East Antarctica. J. Geophys. Res. Oceans 122 (7), 5198-5217.

Liu, C., Wang, Z., Cheng, C., Wu, Y., Xia, R., Li, B., Li, X., 2018. On the Modified Circumpolar Deep Water Upwelling Over the Four Ladies Bank in Prydz Bay, East Antarctica. J. Geophys. Res. Oceans 123 (11), 7819-7838.

MacAyeal, D. R., 1985. Evolution of tidally triggered meltwater plumes below ice shelves. Oceanology of the Antarctic continental shelf 43, 133-143.

Matsumura, Y., Hasumi, H., 2010. Modeling ice shelf water overflow and bottom water formation in the southern Weddell Sea. J. Geophys. Res. Oceans 115 (C10).

Mahoney, A. R., Gough, A. J., Langhorne, P. J., Robinson, N. J., Stevens, C. L., Williams, M. M., Haskell, T. G., 2011. The seasonal appearance of ice shelf water in coastal Antarctica and its effect on sea ice growth. J. Geophys. Res. Oceans 116 (C11).

Marshall, J., Speer, K., 2012. Closure of the meridional overturning circulation through Southern Ocean upwelling. Nat. Geosci. 5 (3), 171.

McPhee, M. G., 1994. On the turbulent mixing length in the oceanic boundary layer. J.

Phys. Oceanogr. 24 (9), 2014-2031.

McCave, I. N., Swift, S. A., 1976. A physical model for the rate of deposition of fine-grained sediments in the deep sea. Geol. Soc. Am. Bull. 87 (4), 541-546.

McConnochie, C. D., & Kerr, R. C. (2018). Dissolution of a sloping solid surface by turbulent compositional convection. J. Fluid Mech. 846, 563-577.

Morse, B., Richard, M., 2009. A field study of suspended frazil ice particles. Cold Reg. Sci. Technol. 55 (1), 86-102.

Mondal, M., Gayen, B., Griffiths, R. W., & Kerr, R. C. (2019). Ablation of sloping ice faces into polar seawater. J. Fluid Mech. 863, 545-571.

Mueller, R. D., Hattermann, T., Howard, S. L., Padman, L., 2018. Tidal influences on a future evolution of the Filchner-Ronne Ice Shelf cavity in the Weddell Sea, Antarctica. Cryosphere 12 (2), 453-476.

Naughten, K. A., Jenkins, A., Holland, P. R., Mugford, R. I., Nicholls, K. W., & Munday, D. R., 2019. Modelling the influence of the Weddell Polynya on the Filchner-Ronne Ice Shelf cavity. J. Climate 32 (16), 5289-5303.

Nicholls, K. W., Jenkins, A., 1993. Temperature and salinity beneath Ronne ice shelf, Antarctica. J. Geophys. Res. Oceans 98 (C12), 22553-22568.

Nicholls, K. W., Makinson, K., Johnson, M. R., 1997. New oceanographic data from beneath Ronne ice shelf, Antarctica. Geophys. Res. Lett. 24 (2), 167-170.

Nicholls, K. W., Makinson, K., & Venables, E. J. (2012). Ocean circulation beneath Larsen C Ice Shelf, Antarctica from in situ observations. Geophys. Res. Lett. 39 (19).

Omstedt, A., Svensson, U., 1984. Modeling supercooling and ice formation in a turbulent Ekman layer. J. Geophys. Res. Oceans 89 (C1), 735-744.

Omstedt, A., 1985. On supercooling and ice formation in turbulent sea-water. J. Glaciol. 31 (109), 263-271.

Orsi, A. H., Johnson, G. C., Bullister, J. L., 1999. Circulation, mixing, and production of Antarctic Bottom Water. Prog. Oceanogr. 43 (1), 55-109.

Owen, P. R., Thomson, W. R., 1963. Heat transfer across rough surfaces. J. Fluid Mech. 15 (3), 321-334.

Pacanowski, R. C., Philander, S. G. H., 1981. Parameterization of vertical mixing in numerical models of tropical oceans. J. Phys. Oceanogr. 11 (11), 1443-1451.

Paolo, F. S., Fricker, H. A., Padman, L., 2015. Volume loss from Antarctic ice shelves is accelerating. Science 348 (6232), 327-331.

Pritchard, H., Ligtenberg, S. R. M., Fricker, H. A., Vaughan, D. G., Van den Broeke, M. R., Padman, L., 2012. Antarctic ice-sheet loss driven by basal melting of ice shelves. Nature 484 (7395), 502-505.

Rees Jones, D., Wells, A, 2018. Frazil-ice growth rate and dynamics in mixed layers and sub-ice-shelf plumes. Cryosphere 12 (1), 25-38.

Rignot, E., Bamber, J. L., Van Den Broeke, M. R., Davis, C., Li, Y., Van De Berg, W. J., Van Meijgaard, E., 2008. Recent Antarctic ice mass loss from radar interferometry and regional climate modelling. Nat. Geosci. 1 (2), 106-110.

Rignot, E., Jacobs, S., Mouginot, J., Scheuchl, B., 2013. Ice-shelf melting around Antarctica. Science 341 (6143), 266-270.

Robinson, N. J., Stevens, C. L., McPhee, M. G., 2017. Observations of amplified roughness from crystal accretion in the sub-ice ocean boundary layer. Geophys. Res. Lett. 44, 1814–1822.

Robinson, N. J., Williams, M. J. M., Barrett, P. J., Pyne, A. R., 2010. Observations of flow and ice-ocean interaction beneath the McMurdo Ice Shelf, Antarctica. J. Geophys. Res. Oceans 115 (C3).

Robinson, N. J., Williams, M. J., Stevens, C. L., Langhorne, P. J., Haskell, T. G., 2014. Evolution of a supercooled Ice Shelf Water plume with an actively growing subice platelet matrix. J. Geophys. Res. Oceans 119 (6), 3425-3446.

Rodi, W., 2017. Turbulence models and their application in hydraulics. Routledge.

Sandhäger, H., Vaughan, D. G., Lambrecht, A., 2004. Meteoric, marine and total ice thickness maps of Filchner-Ronne-Schelfeis, Antarctica. FRISP Rep. 15, 23-30.

Schmidtko, S., Heywood, K. J., Thompson, A. F., Aoki, S., 2014. Multidecadal warming of Antarctic waters. Science 346 (6214), 1227-1231.

Sheng, Y. P., Villaret, C., 1989. Modeling the effect of suspended sediment stratification on bottom exchange processes. J. Geophys. Res. Oceans 94 (C10),

14429-14444.

Silvano, A., Rintoul, S. R., Herraiz-Borreguero, L., 2016. Ocean-ice shelf interaction in East Antarctica. Oceanography 29 (4), 130-143.

Smith, J. D., McLean, S. R., 1977. Spatially averaged flow over a wavy surface. J. Geophys. Res. Oceans 82 (12), 1735-1746.

Smedsrud, L. H., 2002. A model for entrainment of sediment into sea ice by aggregation between frazil-ice crystals and sediment grains. J. Glaciol. 48 (160), 51-61.

Smedsrud, L. H., Jenkins, A., 2004. Frazil ice formation in an ice shelf water plume. J. Geophys. Res. Oceans 109 (C3).

Smetacek, V., Scharek, R., Gordon, L. I., Eicken, H., Fahrbach, E., Rohardt, G., Moore, S., 1992. Early spring phytoplankton blooms in ice platelet layers of the southern Weddell Sea, Antarctica. Deep-Sea Res. Pt I 39 (2), 153-168.

Soulsby,R.L.,1983.The bottom boundary layer of shelf seas. In: Johns, B. (Ed.), Physical Oceanography of Coastal and Shelf Seas. Elsevier Science Publishers B.V., Amster-dam, pp. 189-26.

Stanton, T. P., Shaw, W. J., Truffer, M., Corr, H. F. J., Peters, L. E., Riverman, K. L., Bindschadler, R., Holland, D. M., Anandakrishnan, S., 2013. Channelized ice melting in the ocean boundary layer beneath Pine Island Glacier, Antarctica. Science 341 (6151), 1236-1239.

Tsang, G., Hanley, T. O. D., 1985. Frazil formation in water of different salinities and supercoolings. J. Glaciol. 31 (108), 74-85.

Vanoni, V. A., 1946. Transportation of suspended sediment by water. Trans. of ASCE 111, 67-102.

Valiani, A., 1988. An open question regarding shear flow with suspended sediments. Meccanica 23 (1), 36-43.

Villaret, C., Trowbridge, J. H., 1991. Effects of stratification by suspended sediments on turbulent shear flows. J. Geophys. Res. Oceans 96 (C6), 10659-10680.

Vreugdenhil, C. A., Taylor, J. R., 2019. Stratification effects in the turbulent boundary layer beneath a melting ice shelf: Insights from resolved large-eddy simulations.

J. Phys. Oceanogr. 49 (7), 1905-1925.

Winterwerp, J. C., 2001. Stratification effects by cohesive and noncohesive sediment. J. Geophys. Res. Oceans 106 (C10), 22559-22574.

Winterwerp, J. C., 2006. Stratification effects by fine suspended sediment at low, medium, and very high concentrations. J. Geophys. Res. Oceans 111 (C5).

Williams, G. D., Herraiz-Borreguero, L., Roquet, F., Tamura, T., Ohshima, K. I., Fukamachi, Y., Fraser, A. D., Gao, L., Chen, H., McMahon, C. R., Harcourt, R., Hindell, M., 2016. The suppression of Antarctic bottom water formation by melting ice shelves in Prydz Bay. Nat. Commun. 7, 12577.

Wolanski, E., Chappell, J., Ridd, P., Vertessy, R., 1988. Fluidization of mud in estuaries. J. Geophys. Res. Oceans 93 (C3), 2351-2361.

Wright, S., Parker, G., 2004. Density stratification effects in sand-bed rivers. J. Hydraul. Eng. 130 (8), 783-795.

Yaglom, A. M., Kader, B. A., 1974. Heat and mass transfer between a rough wall and turbulent fluid flow at high Reynolds and Peclet numbers. J. Fluid Mech. 62 (3), 601-623.

Table 1

List of parameters used in Reference run.

Parameter	Value	Description
ϕ	$-1.362 \times 10^{-4}\ \mathrm{s}^{-1}$	Coriolis parameter
$\mathrm{N_i}$	6	Number of frazil-ice sizes
$\mathrm{r_{i,1}}, \mathrm{r_{i,2}}, \ldots, \mathrm{r_{i,6}}$	0.03, 0.1, 0.3, 0.5, 0.7, 0.9 mm	Frazil ice radii for each class
$\mathrm{a_r}$	0.02	Aspect ratio of frazil discs
$\bar{\mathrm{n}}$	$1 \times 10^{3}\ \mathrm{m}^{-3}$	Average number of frazil crystals in all size classes per unit volume
k_s	0.03 m	Equivalent roughness height
$\mathrm{A_{z,min}}$	$3 \times 10^{-3}\ \mathrm{m}^{2}.\mathrm{s}^{-1}$	Minimum eddy viscosity*

*Not applied for $\mathrm{A_{z0}}$

1022 **Figure 1**

1023

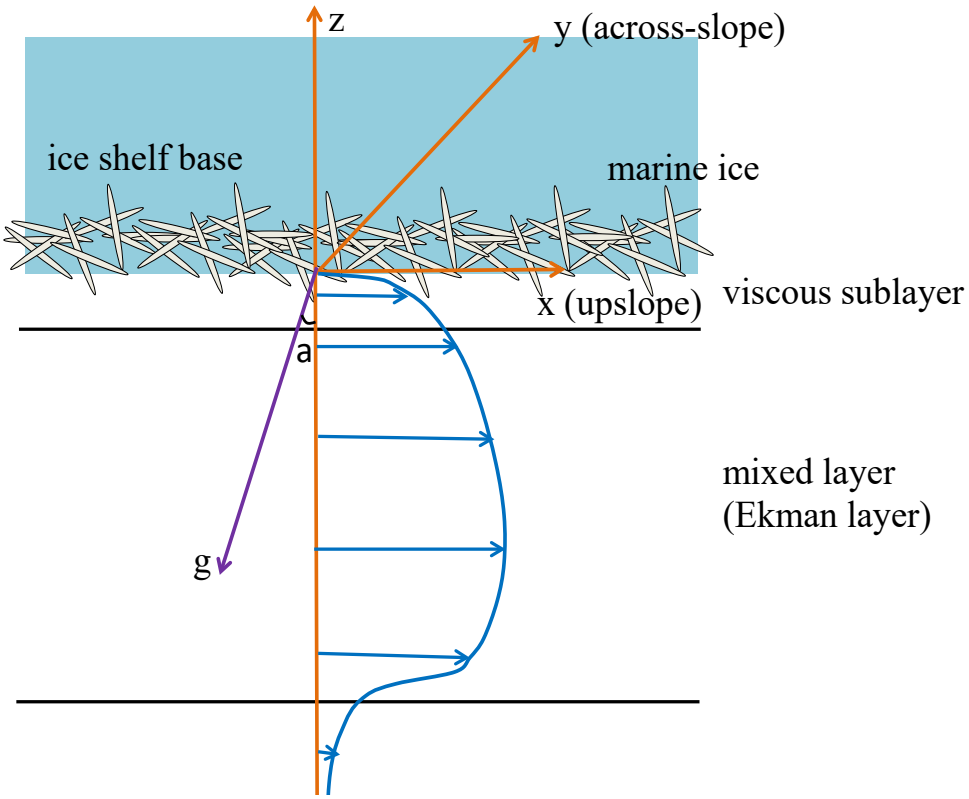
z
y (across-slope)
ice shelf base
marine ice
x (upslope)
viscous sublayer
a
mixed layer
(Ekman layer)
g

1026 **Figure 2**

1027

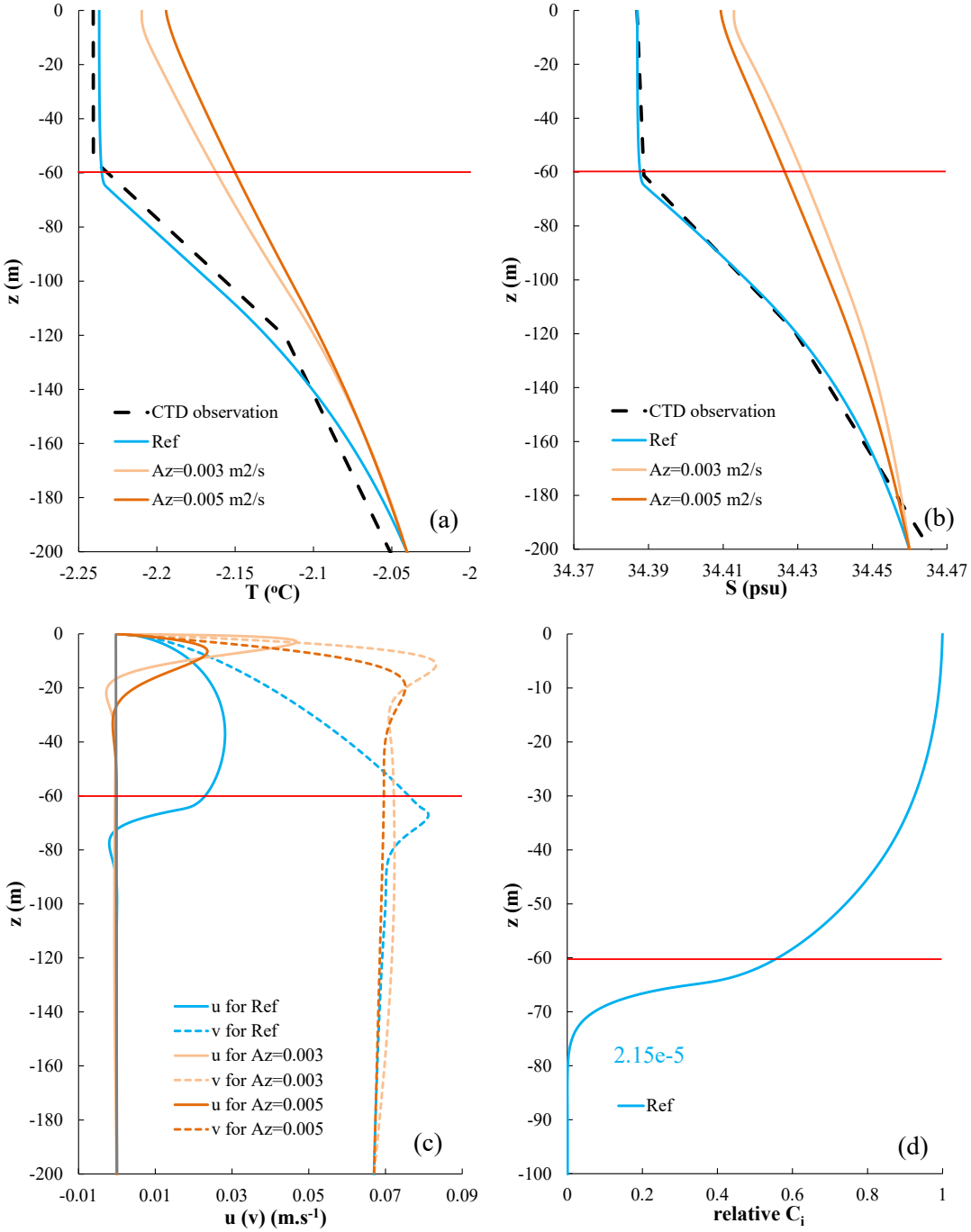
z (m)
T (°C)
CTD observation
Ref
Az=0.003 m2/s
Az=0.005 m2/s
(a)
S (psu)
(b)
u (v) (m.s-1)
u for Ref
v for Ref
u for Az=0.003
v for Az=0.003
u for Az=0.005
v for Az=0.005
(c)
relative Ci
2.15e-5
(d)

1030 **Figure 3**

1031

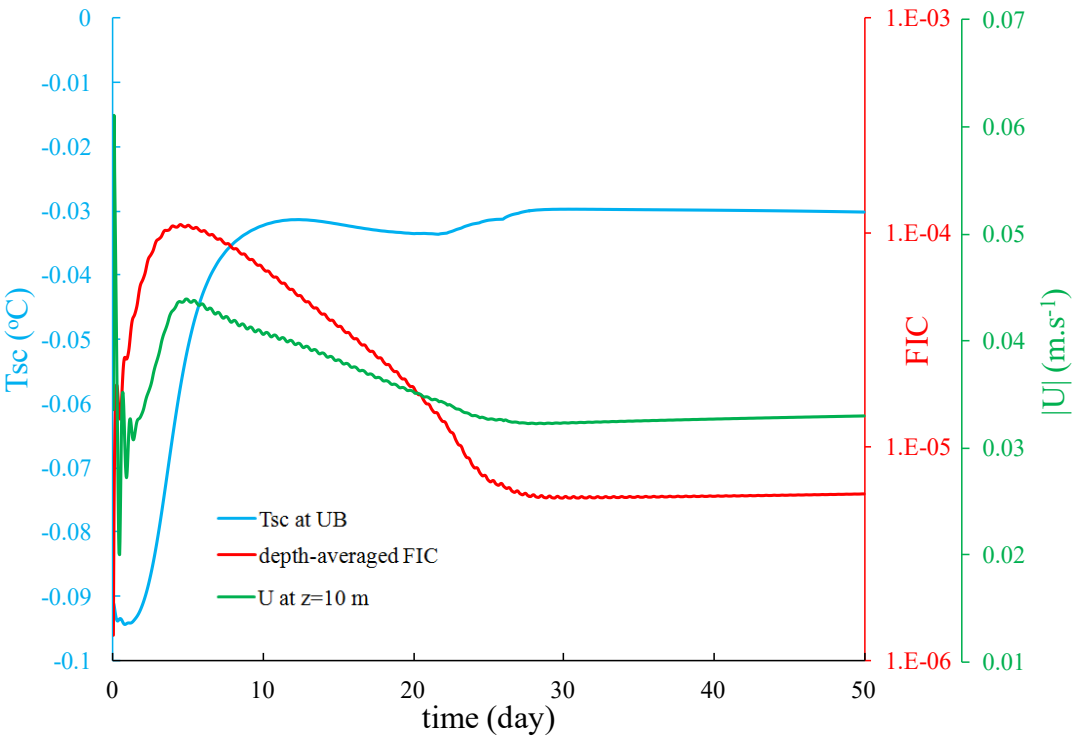
0
-0.01
-0.02
-0.03
-0.04
-0.05
-0.06
-0.07
-0.08
-0.09
-0.1
Tsc (°C)
1.E-03
1.E-04
1.E-05
1.E-06
FIC
0.07
0.06
0.05
0.04
0.03
0.02
0.01
|U| (m.s-1)
Tsc at UB
depth-averaged FIC
U at z=10 m
0
10
20
30
40
50
time (day)

1034 **Figure 4**

1035

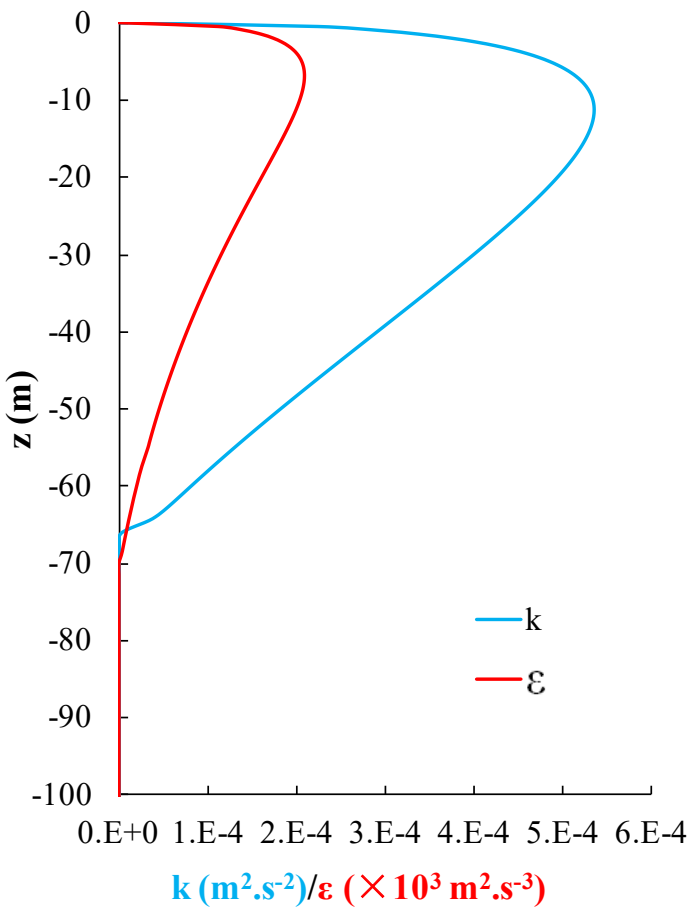
0
-10
-20
-30
-40
-50
-60
-70
-80
-90
-100
z (m)
k
ε
0.E+0
1.E-4
2.E-4
3.E-4
4.E-4
5.E-4
6.E-4
k (m².s⁻²)/ε (×10³ m².s⁻³)

1038 **Figure 5**

1039

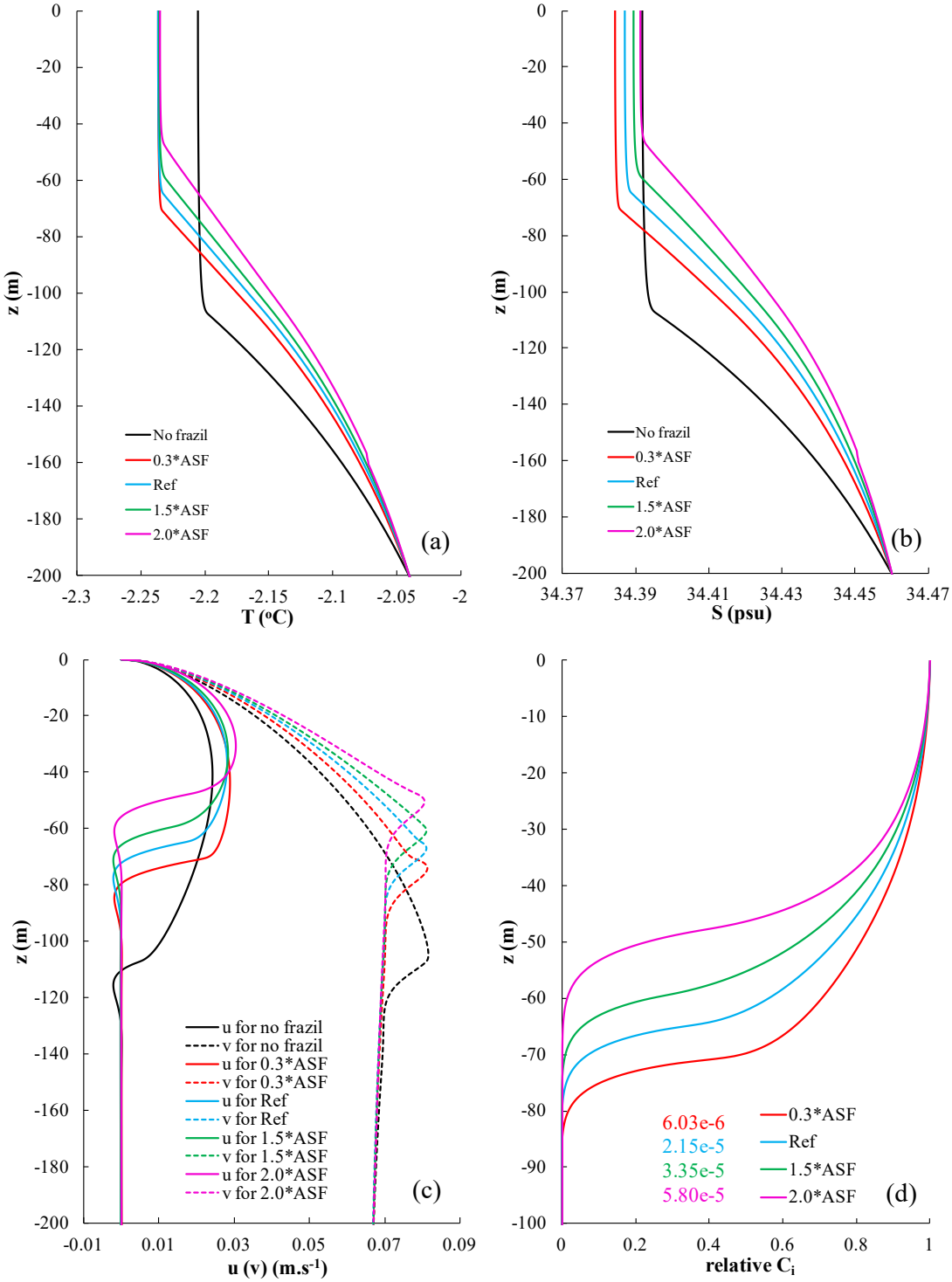
z (m)
T (ºC)
No frazil
0.3*ASF
Ref
1.5*ASF
2.0*ASF
(a)
S (psu)
(b)
u (v) (m.s-1)
u for no frazil
v for no frazil
u for 0.3*ASF
v for 0.3*ASF
u for Ref
v for Ref
u for 1.5*ASF
v for 1.5*ASF
u for 2.0*ASF
v for 2.0*ASF
(c)
relative Ci
6.03e-6
2.15e-5
3.35e-5
5.80e-5
(d)

1042 **Figure 6**

1043

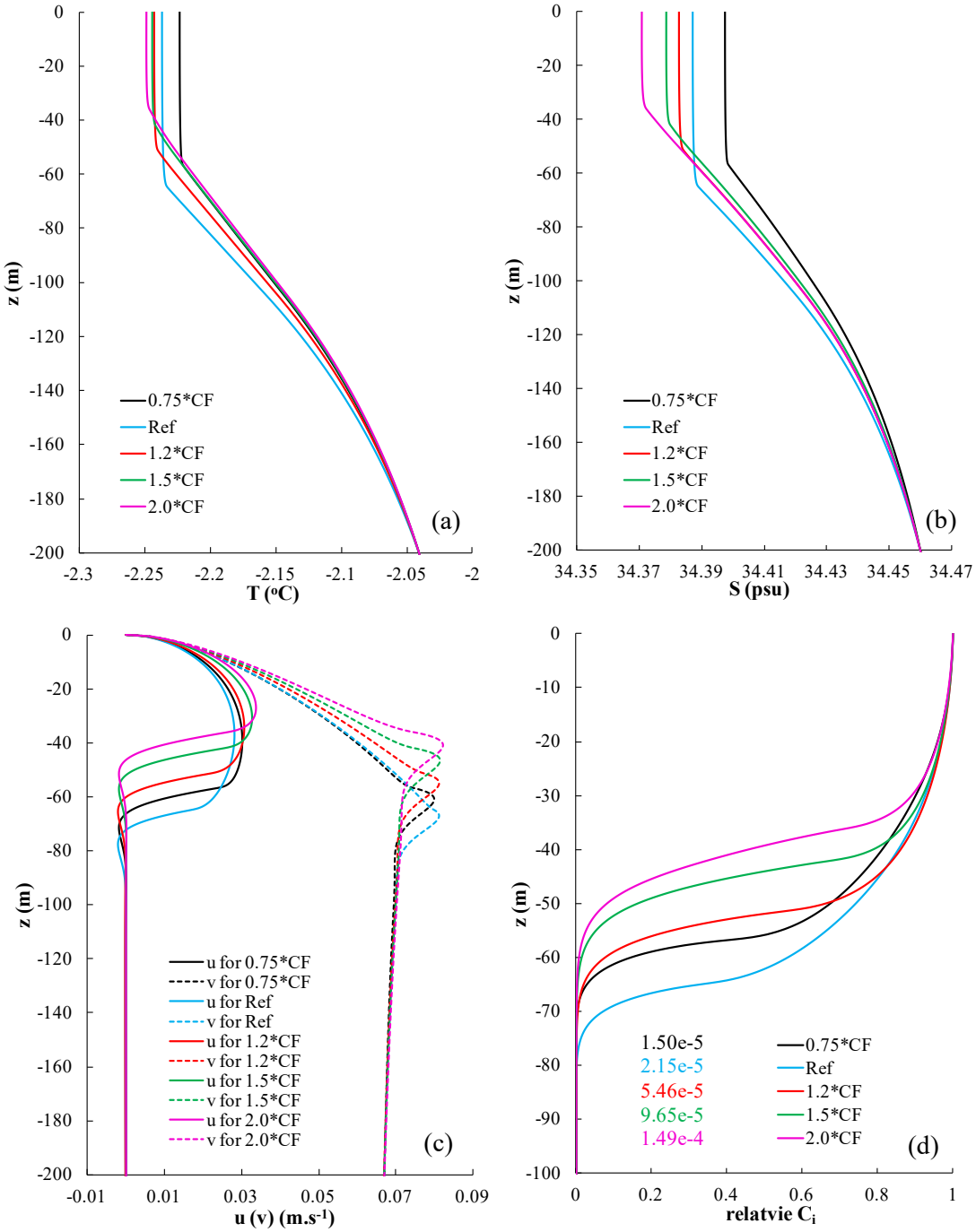
z (m)
T (°C)
0.75*CF
Ref
1.2*CF
1.5*CF
2.0*CF
(a)
S (psu)
(b)
u (v) (m.s-1)
u for 0.75*CF
v for 0.75*CF
u for Ref
v for Ref
u for 1.2*CF
v for 1.2*CF
u for 1.5*CF
v for 1.5*CF
u for 2.0*CF
v for 2.0*CF
(c)
relatvie Ci
1.50e-5
2.15e-5
5.46e-5
9.65e-5
1.49e-4
(d)

1046 **Figure 7**

1047

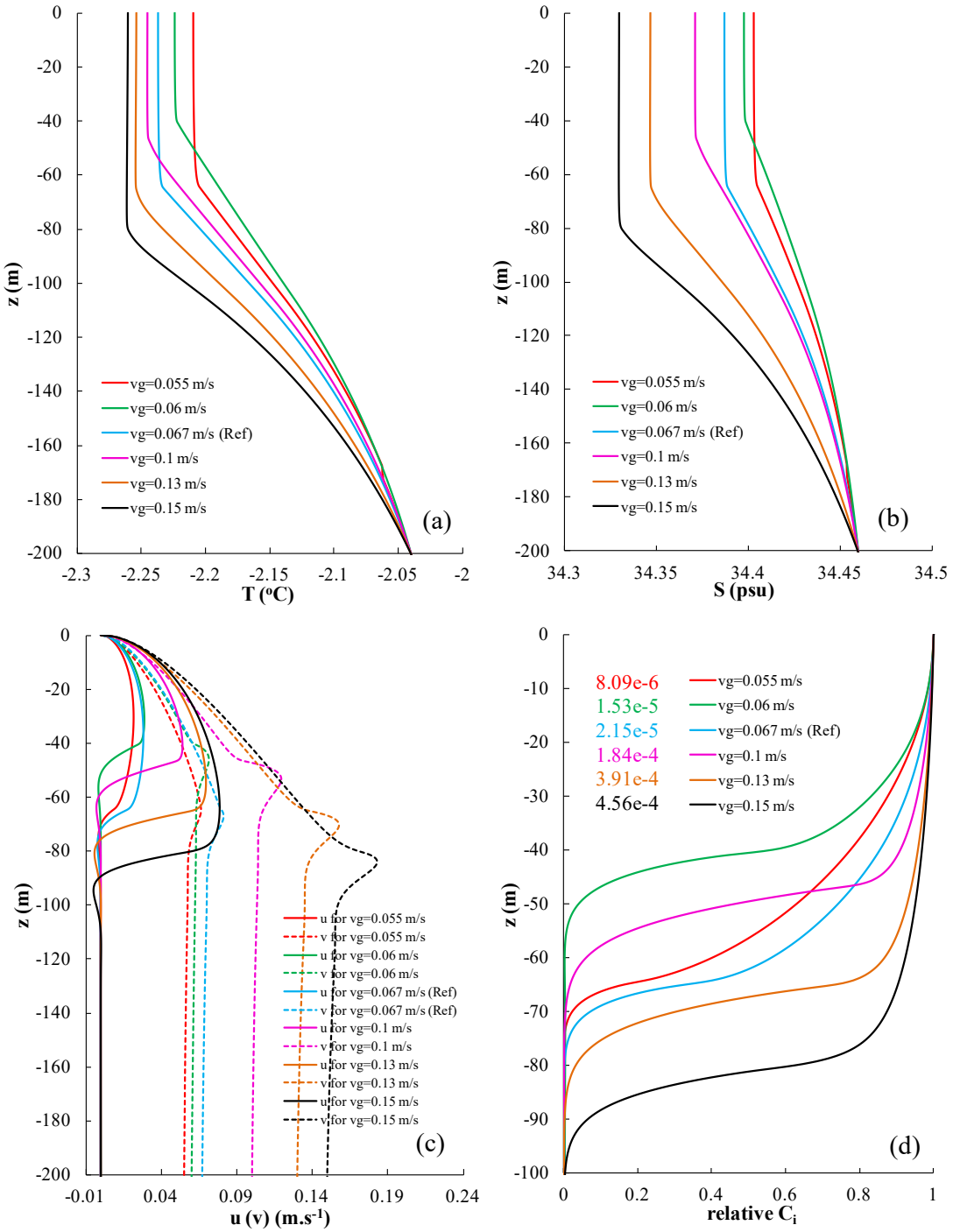
(a)
z (m)
T (°C)
vg=0.055 m/s
vg=0.06 m/s
vg=0.067 m/s (Ref)
vg=0.1 m/s
vg=0.13 m/s
vg=0.15 m/s
(b)
S (psu)
(c)
u (v) (m.s-1)
u for vg=0.055 m/s
v for vg=0.055 m/s
u for vg=0.06 m/s
v for vg=0.06 m/s
u for vg=0.067 m/s (Ref)
v for vg=0.067 m/s (Ref)
u for vg=0.1 m/s
v for vg=0.1 m/s
u for vg=0.13 m/s
v for vg=0.13 m/s
u for vg=0.15 m/s
v for vg=0.15 m/s
(d)
relative Ci
8.09e-6
1.53e-5
2.15e-5
1.84e-4
3.91e-4
4.56e-4

1050 **Figure 8**

1051

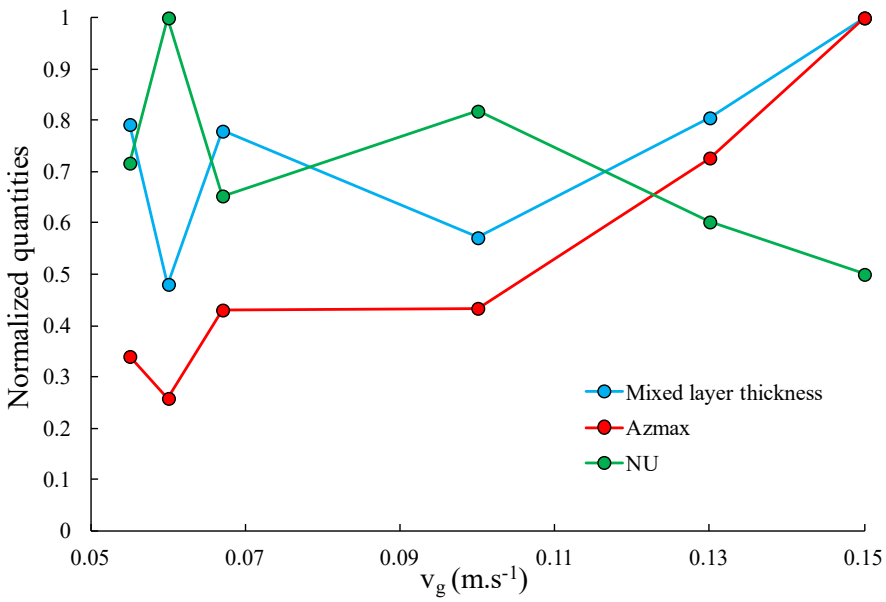
Normalized quantities
1
0.9
0.8
0.7
0.6
0.5
0.4
0.3
0.2
0.1
0
0.05
0.07
0.09
0.11
0.13
0.15
v_g (m.s^{-1})
Mixed layer thickness
Azmax
NU

Figure 9

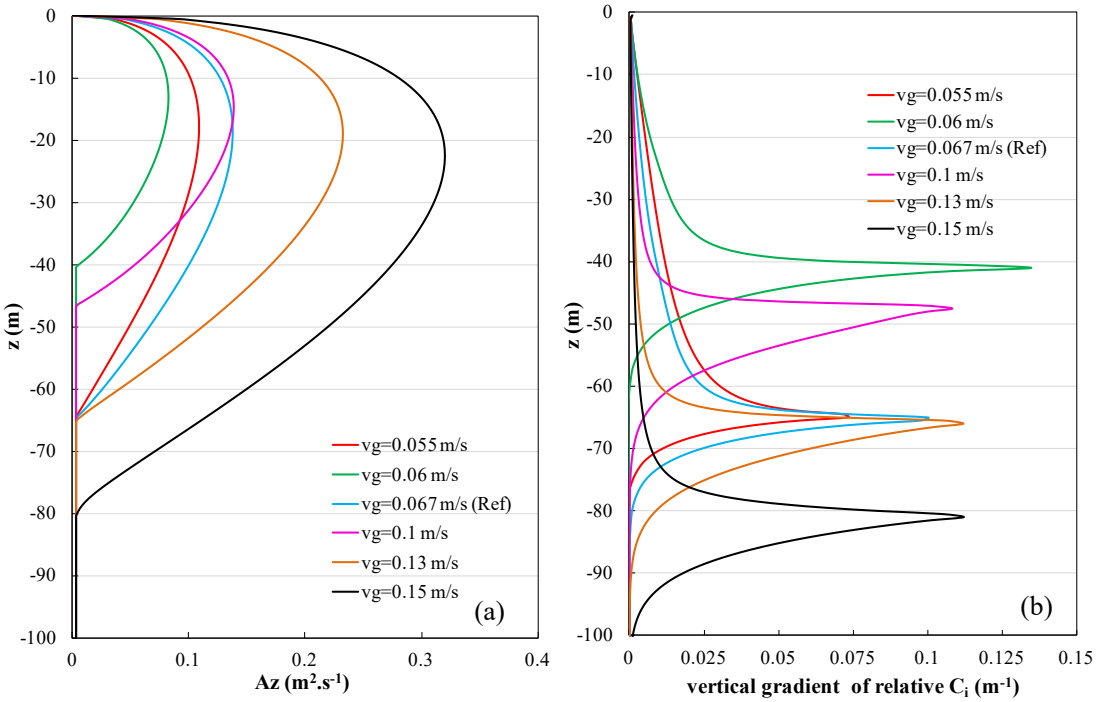
0
-10
-20
-30
-40
-50
-60
-70
-80
-90
-100
z (m)
0
0.1
0.2
0.3
0.4
Az (m².s⁻¹)
vg=0.055 m/s
vg=0.06 m/s
vg=0.067 m/s (Ref)
vg=0.1 m/s
vg=0.13 m/s
vg=0.15 m/s
(a)
0
0.025
0.05
0.075
0.1
0.125
0.15
vertical gradient of relative Ci (m⁻¹)
(b)

1058 **Figure 10**

1059

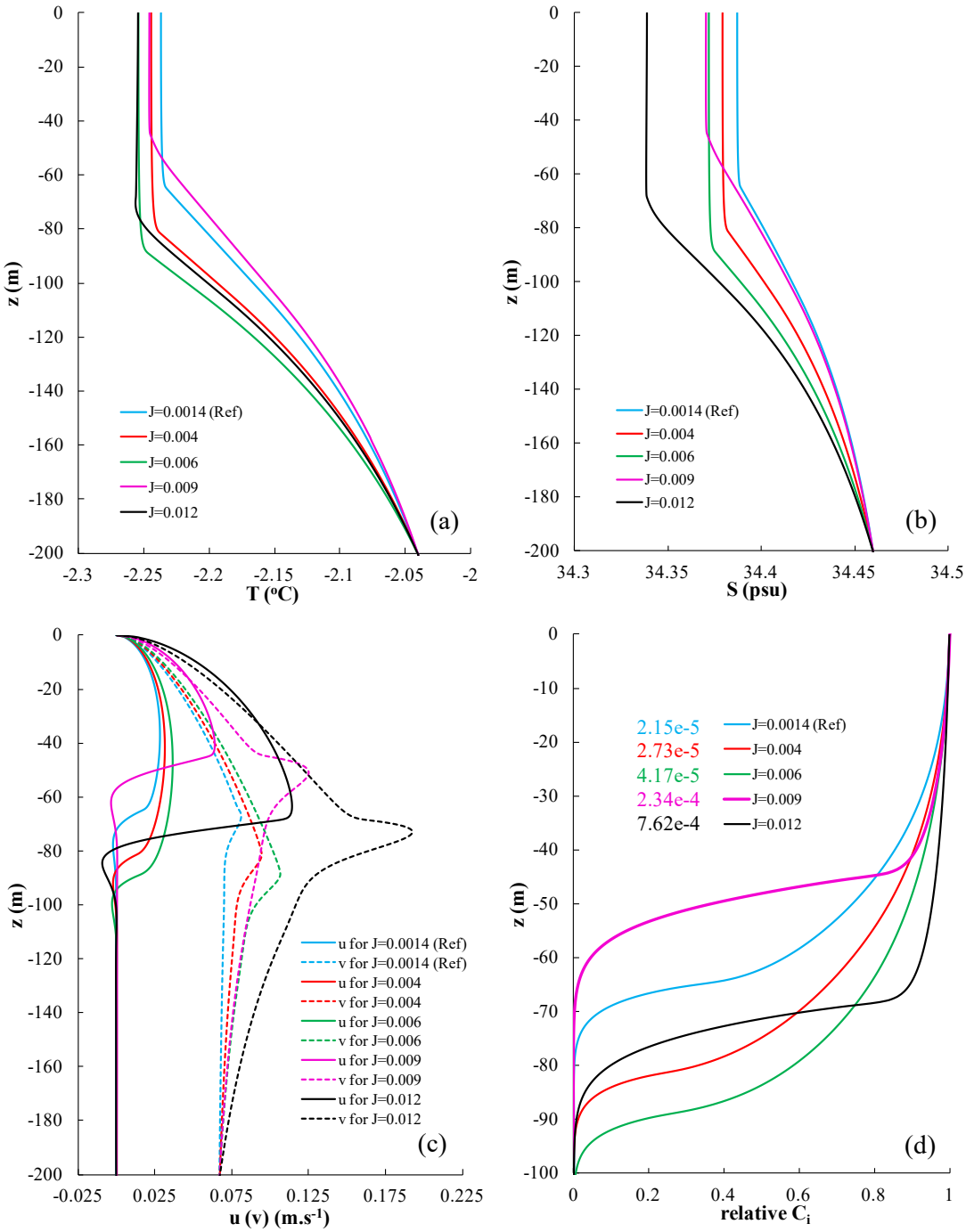
z (m)
T (ºC)
J=0.0014 (Ref)
J=0.004
J=0.006
J=0.009
J=0.012
(a)
S (psu)
(b)
u (v) (m.s-1)
u for J=0.0014 (Ref)
v for J=0.0014 (Ref)
u for J=0.004
v for J=0.004
u for J=0.006
v for J=0.006
u for J=0.009
v for J=0.009
u for J=0.012
v for J=0.012
(c)
relative Ci
2.15e-5
2.73e-5
4.17e-5
2.34e-4
7.62e-4
(d)

1062 **Figure 11**

1063

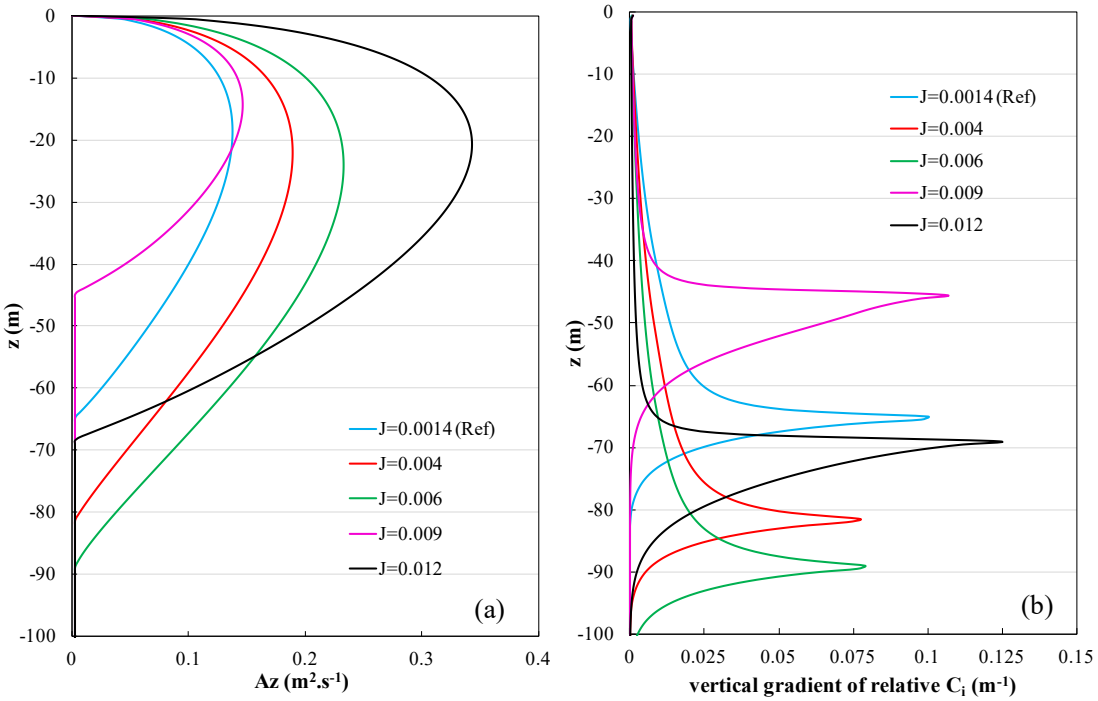
0
-10
-20
-30
-40
-50
-60
-70
-80
-90
-100
z (m)
0
0.1
0.2
0.3
0.4
Az (m².s⁻¹)
J=0.0014 (Ref)
J=0.004
J=0.006
J=0.009
J=0.012
(a)
0
0.025
0.05
0.075
0.1
0.125
0.15
vertical gradient of relative Ci (m⁻¹)
(b)

1066 **Figure 12**

1067

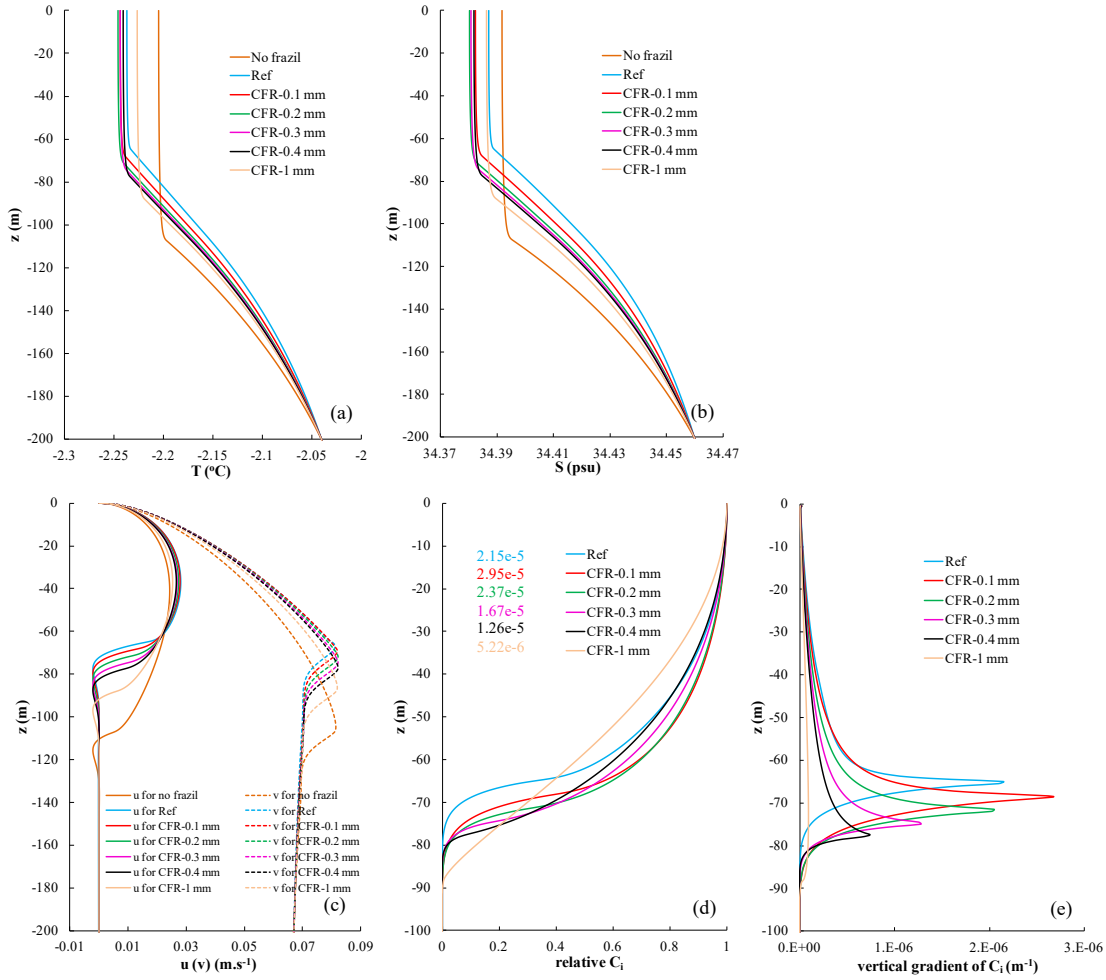
No frazil
Ref
CFR-0.1 mm
CFR-0.2 mm
CFR-0.3 mm
CFR-0.4 mm
CFR-1 mm
z (m)
T (ºC)
(a)
S (psu)
(b)
u for no frazil
u for Ref
u for CFR-0.1 mm
u for CFR-0.2 mm
u for CFR-0.3 mm
u for CFR-0.4 mm
u for CFR-1 mm
v for no frazil
v for Ref
v for CFR-0.1 mm
v for CFR-0.2 mm
v for CFR-0.3 mm
v for CFR-0.4 mm
v for CFR-1 mm
u (v) (m.s-1)
(c)
2.15e-5
2.95e-5
2.37e-5
1.67e-5
1.26e-5
5.22e-6
relative Ci
(d)
vertical gradient of Ci (m-1)
(e)

1070 **Figure 13**

1071

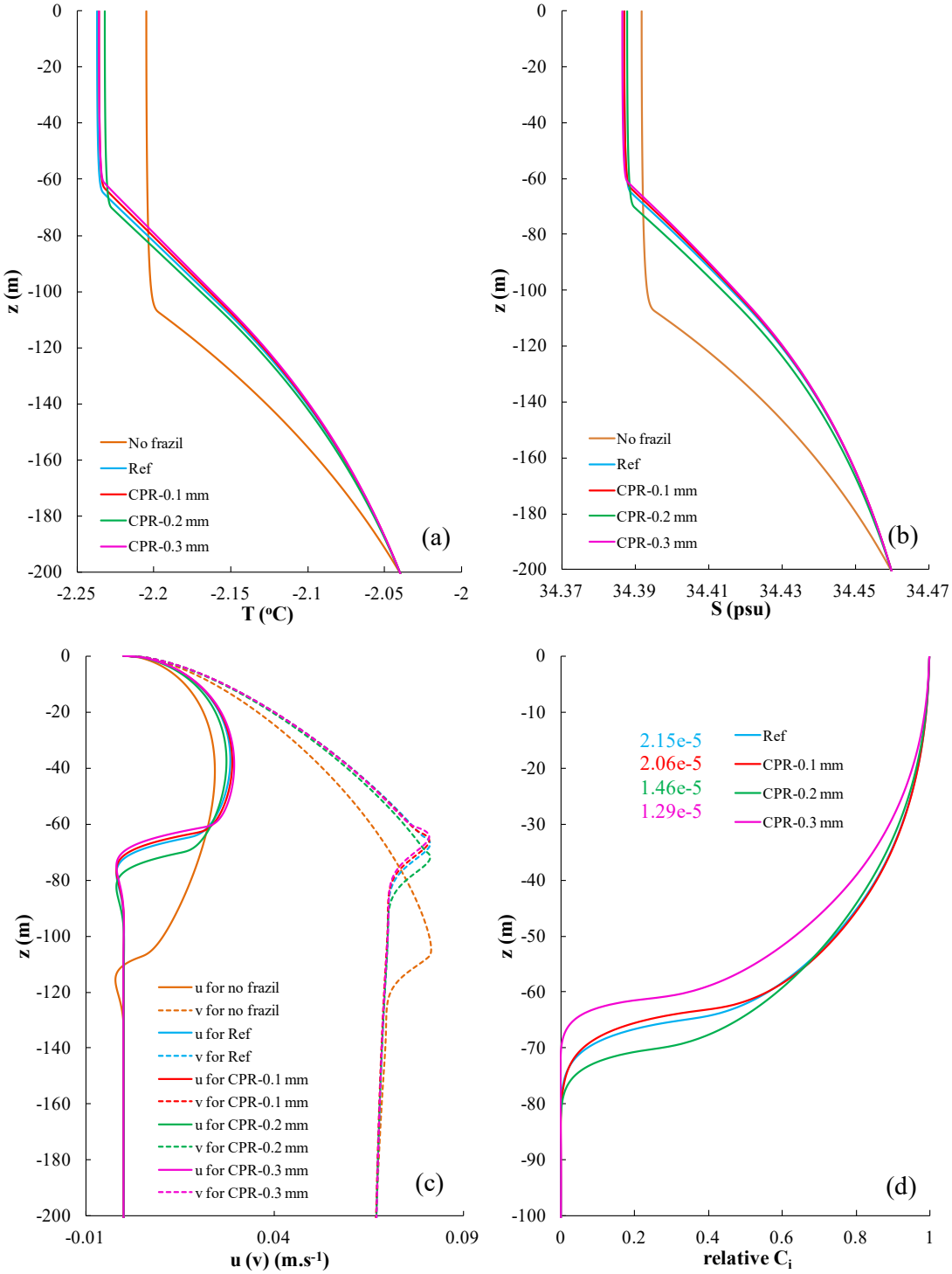
z (m)
T (ºC)
No frazil
Ref
CPR-0.1 mm
CPR-0.2 mm
CPR-0.3 mm
(a)
S (psu)
(b)
u (v) (m.s-1)
u for no frazil
v for no frazil
u for Ref
v for Ref
u for CPR-0.1 mm
v for CPR-0.1 mm
u for CPR-0.2 mm
v for CPR-0.2 mm
u for CPR-0.3 mm
v for CPR-0.3 mm
(c)
relative Ci
2.15e-5
2.06e-5
1.46e-5
1.29e-5
(d)

1074 **Figure 14**

1075

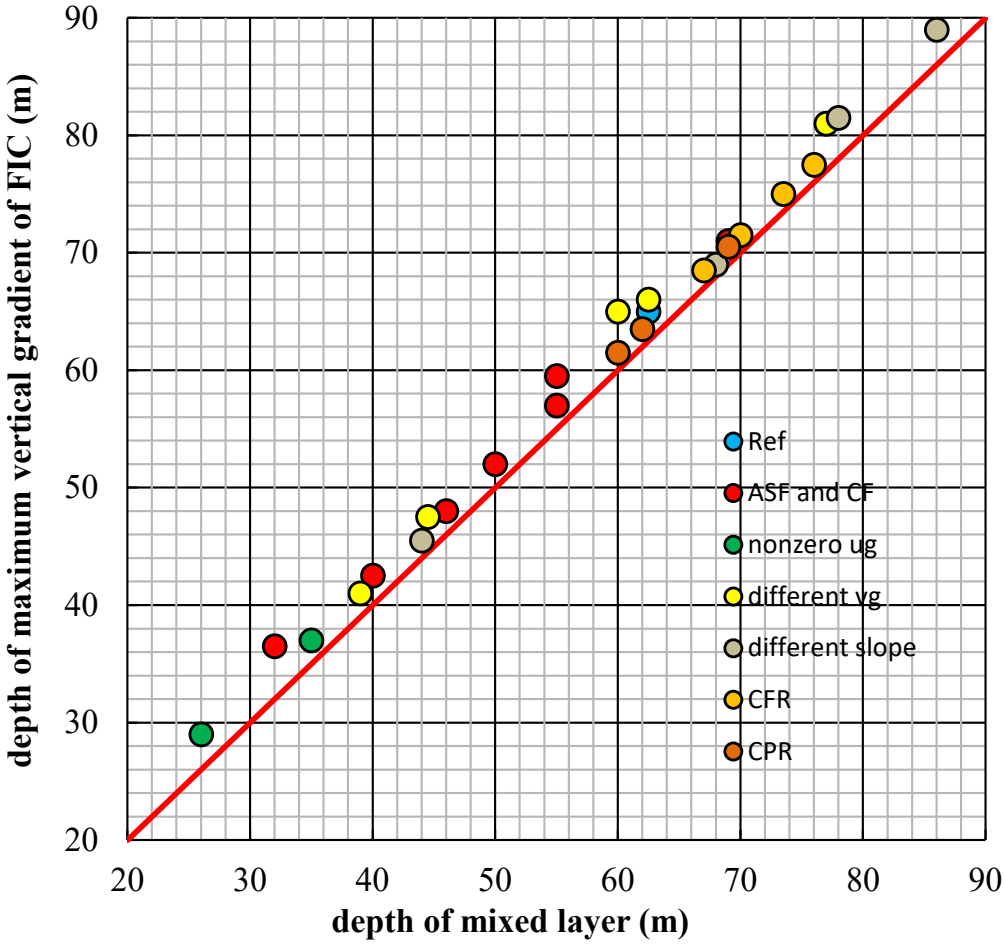
depth of maximum vertical gradient of FIC (m)
depth of mixed layer (m)
20
30
40
50
60
70
80
90
Ref
ASF and CF
nonzero ug
different vg
different slope
CFR
CPR

1078 **Figure 15**

1079

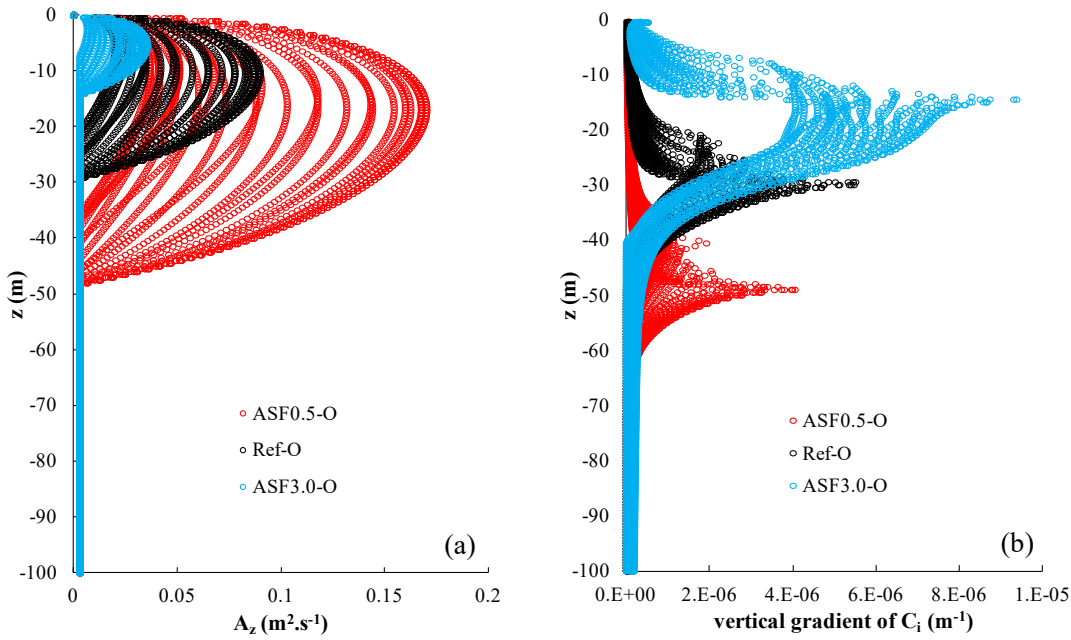
0
-10
-20
-30
-40
-50
-60
-70
-80
-90
-100
z (m)
ASF0.5-O
Ref-O
ASF3.0-O
(a)
0
0.05
0.1
0.15
0.2
A_z (m^2.s^{-1})
(b)
0.E+00
2.E-06
4.E-06
6.E-06
8.E-06
1.E-05
vertical gradient of C_i (m^{-1})

1082 **Figure 16**

1083

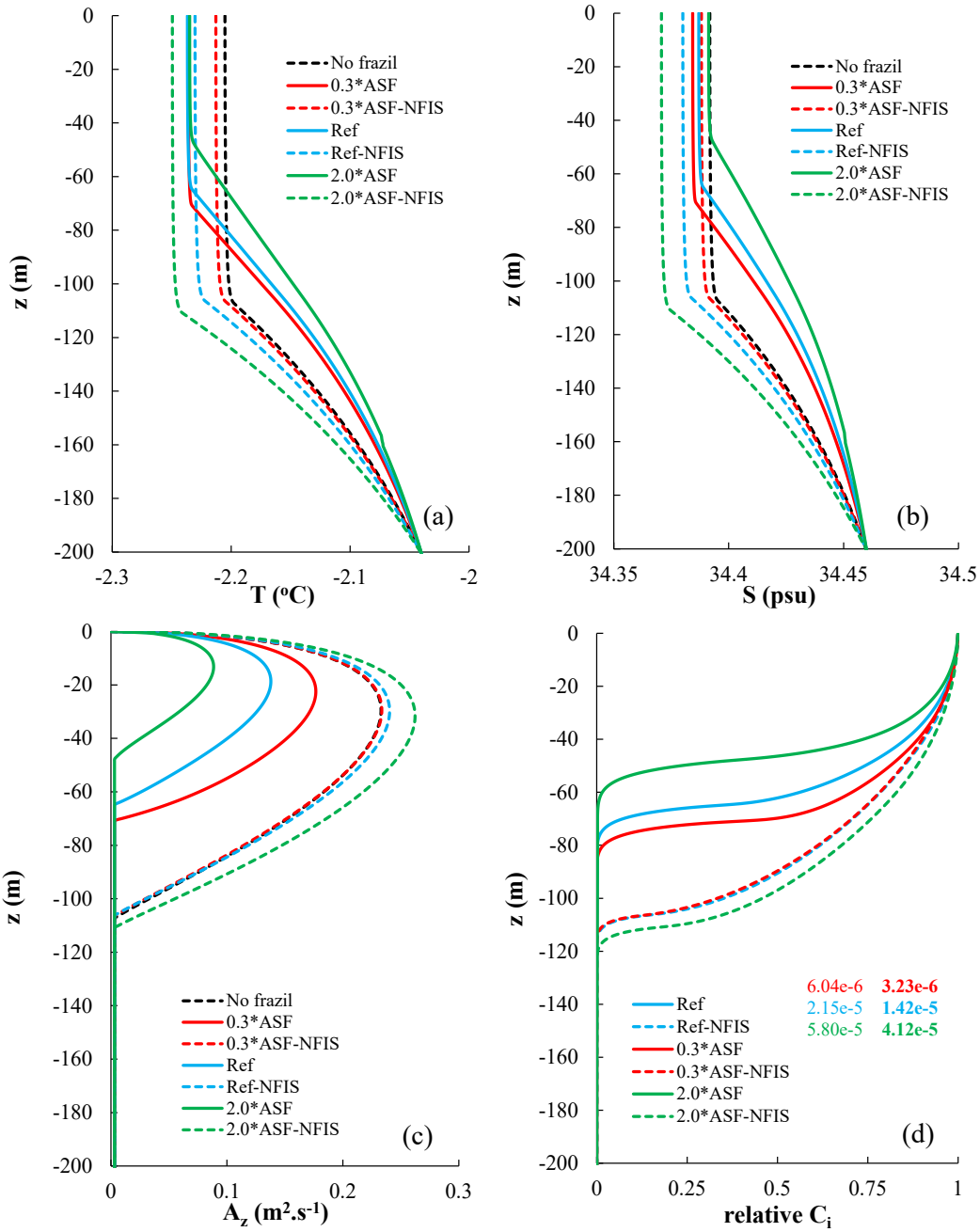
No frazil
0.3*ASF
0.3*ASF-NFIS
Ref
Ref-NFIS
2.0*ASF
2.0*ASF-NFIS
z (m)
T (ºC)
(a)
S (psu)
(b)
A_z ($m^2.s^{-1}$)
(c)
relative C_i
6.04e-6 3.23e-6
2.15e-5 1.42e-5
5.80e-5 4.12e-5
(d)

1084